

PAPER

CVD grown nitrogen doped graphene is an exceptional visible-light driven photocatalyst for surface catalytic reactions

To cite this article: Kazi M Alam *et al* 2020 *2D Mater.* 7 015002

View the [article online](#) for updates and enhancements.

2D Materials



PAPER







CVD grown nitrogen doped graphene is an exceptional visible-light driven photocatalyst for surface catalytic reactions

RECEIVED
1 July 2019

REVISED
8 September 2019

ACCEPTED FOR PUBLICATION
17 September 2019

PUBLISHED
4 October 2019

Kazi M Alam¹, Pawan Kumar¹ , Ajay P Manuel¹ , Ehsan Vahidzadeh¹ , Ankur Goswami¹, Sheng Zeng¹ , Wenjie Wu^{3,4}, Najia Mahdi¹, Kai Cui², Alexander E Kobryn², Sergey Gusarov², Yanan Song^{3,4,5} , and Karthik Shankar^{1,4,5} 

¹ Department of Electrical and Computer Engineering, University of Alberta, 9211-116 St., Edmonton, AB T6G 1H9, Canada

² Nanotechnology Research Centre, National Research Council Canada, 11421 Saskatchewan Drive, Edmonton, AB T6G 2M9, Canada

³ Engineering Research Center for Nanophotonics and Advanced Instrument, School of Physics and Electronic Science, East China Normal University, Shanghai 200062, People's Republic of China

⁴ Joint Institute of Advanced Science and Technology, East China Normal University, Shanghai 200062, People's Republic of China

⁵ Author to whom any correspondence should be addressed.

E-mail: kshankar@ualberta.ca and ynsong@phy.ecnu.edu.cn

Keywords: exciton plasmon coupling, hot electron injection, plasmon induced resonance energy transfer, photoreduction, FDTD simulations, plasmonic catalysis, van der Waals materials

Supplementary material for this article is available [online](#)

Abstract

The photocatalytic potential of large area CVD grown nitrogen doped graphene (NGr) has been explored through the chemical transformation of 4-nitrobenzene thiol into p,p'-dimercaptoazobenzene. Decoration of NGr with Ag nanocubes with rounded edges to form NGr/Ag nanohybrids resulted in a slight increase in the work-function and a decrease in the n-type character of NGr due to ground state transfer of negative charge from NGr to Ag. The Ag nanocubes exhibited a localized surface plasmon resonance (LSPR) at ~425 nm. When the NGr/Ag nanohybrids were illuminated with visible light of wavelength close to the LSPR peak, Kelvin probe force microscopy (KPFM) indicated a dramatic change in surface potential of -225 mV and Raman spectra detected electron accumulation in NGr, which are attributed to a high local field enhancement-mediated hot electron injection into NGr and the formation of long-lived charge separated states. Pristine nitrogen doped graphene and its coupled system with plasmonic Ag nanoparticles showed superior photocatalytic performance compared to bare plasmonic Ag catalyst. While standalone Ag NPs were unable to complete the transformation of 4-NBT into DMAB even at a laser power of 10 mW, NGr/Ag nanohybrids completed this transformation at a laser power of 1 mW, pointing to the high photoreduction strength of NGr/Ag. Density functional theory (DFT) based computational modeling was used to examine the electronic structure of graphene doped with graphitic, pyridinic and pyrrolic nitrogen dopant atoms. DFT results indicated an enhanced chemical reactivity of NGr due to stronger localization of charge at the dopant sites and a pronounced difference in the projected density of states (PDOS) for carbon atoms in proximity to, and distant from, the nitrogen dopant sites.

1. Introduction

Graphene, a single atom-thick two-dimensional (2D) sheet of sp^2 hybridized carbon atoms, has been extensively studied experimentally and theoretically, due to its distinct electronic properties governed by the relativistic quantum mechanical Dirac equation [1, 2]. Graphene has long range π -conjugation and can be considered as the basic building block of all other

carbon-based allotropes that are comprised of sp^2 hybridized carbon atoms. Since its discovery, it has been explored by many research groups around the globe, in order to advance the fundamental science of 2D materials and unveil technological potential [3]. However pristine graphene is a zero-band gap semiconductor possessing semimetallic character, which renders it ineffective as a standalone photocatalyst. Incorporation of an impurity

heteroatom through compositional doping is an effective route to alter the electronic properties of graphene. Such behavior modification is desirable for a plethora of applications; for instance, chemical doping increases the on/off current ratio of a graphene-based transistor [4]. A nitrogen atom has one extra electron than a carbon atom, and analogous atomic size. Therefore N-doping of graphene is a viable way to tune the electronic properties of graphene without compromising its high mobility [4–9]. Both experimental and theoretical works showed an upward shifting of the Fermi level relative to the Dirac point in N-doped graphene (NGr), giving rise to a finite bandgap in this *n*-type semiconductor [5–7, 10]. In addition to the creation of a bandgap, nitrogen doping modifies the charge distribution over the carbon atoms and increases chemical reactivity through creation of catalytically active sites, thus making it suitable as a catalyst [6,7].

NGr has been demonstrated to have potential applications in many fields of current technological interest, particularly those related to energy research. In non-energy related fields, NGr has been used in field-effect transistors [11–14], electrochemical biosensors and medical devices [15, 16], nonvolatile memories [17], and light emitting diodes [18]. Insofar as energy-related applications are concerned, NGr has been used in lithium ion batteries [19, 20], as an electrocatalyst in fuel-cells [21, 22], and in supercapacitors [21, 23]. However, research papers on the potential of NGr in solar energy harvesting devices, such as photocatalysts, are surprisingly scarce [7, 8, 24, 25]. Jia *et al* reported CdS/NGr composite photocatalyst for photoelectrochemical water splitting [25], where NGr plays the role of a co-catalyst, anchoring CdS nanocrystals on its 2D honeycomb nanosheet and enhances photogenerated electron–hole separation under visible light illumination [25]. Here in this communication, we report the photocatalytic performance of stand-alone NGr and its composite with lab-grown Ag nanoparticles in the surface chemical transformation of 4-nitrobenzenethiol (4-NBT) into *p,p'*-dimercaptoazobenzene (DMAB) under visible light. To the best of our knowledge this is the first report on the photocatalytic performance of pristine 2D NGr and Ag/NGr hybrid.

In a semiconductor-noble metal nanocomposite, the bound electron hole pair (exciton) in the semiconductor and the surface plasmon in the noble metal can interact with each other to form a plexciton provided the illumination wavelength is such that both species are photo-excited. In this study, the photocatalytic activity of both excitonic (NGr) and plexcitonic (Ag/NGr) systems have been studied and compared with plasmonic pristine silver nanoparticles [26]. Photo-conversion of 4-NBT to DMAB is a reduction reaction that has been observed on plasmonic metal surfaces such as Ag, Au and Cu [27], in hybrid systems comprising noble plasmonic particles such as Ag, and semiconductor photocatalysts such as TiO₂ [28],

MoS₂ [29], and graphene oxide [30]. Strong exciton-plasmon coupling has been experimentally observed in Ag nanowire and graphene composite system [26]. The exciton plasmon co-driven photochemical transformation under visible wavelength laser illumination is a consequence of coupling between generated surface plasmons at the metal nanoparticle/semiconductor interfaces with the photogenerated excitons in the semiconductor. Ag nanowire-graphene composite system showed a huge accumulation of hot electrons as well as increased plasmon to electron conversion efficiency caused by strong plasmon–exciton coupling [26]. Recently plexcitonics has become an active field of research since it holds great promise for solar energy harvesting applications [31]. We have chosen Ag nanoparticles due to their low intrinsic loss that gives rise to a narrow localized surface plasmon resonance (LSPR) with large electromagnetic field enhancement [32]. Both the Ag/NGr and pristine NGr systems showed superior performances in driving photocatalytic reactions through plexcitonic and excitonic effects respectively, compared to the pristine Ag nanoparticles that utilizes the plasmonic effect alone.

Although solution based techniques have been used to form graphene flakes, NGr and their heterojunctions [33–38], the highest quality graphene is still primarily obtained by chemical vapor deposition (CVD) on catalytic metal substrates. The extended delocalization of π -electrons in large area CVD-grown NGr has enabled electron mobilities of 1000 cm² V⁻¹ s⁻¹ to 9000 cm² V⁻¹ s⁻¹ to be measured in such NGr films [39, 40]. Herein we used CVD-grown NGr to form hybrids with Ag nanocubes.

2. Experimental details

2.1. Synthesis of large area nitrogen doped graphene

Nitrogen doped graphene was grown on copper foil (Alfa Aesar, purity of 99.8%, and thickness of 25 μ m). A low pressure chemical vapor deposition (LPCVD) process was used with the pressure under 1 Pa in the furnace at the initial stage. 10 sccm H₂ (purity of 99.999%) was introduced into the furnace tube with the pressure of 12 Pa, and the system was heated to 1000 °C in 1.5 h. Then the temperature was held for 100 min to anneal the copper substrate. Acetonitrile was used as the carbon source and nitrogen source. The acetonitrile was evaporated from a stainless steel tank using a pump, and the pressure of acetonitrile was controlled using a pressure meter. The growth temperature and hydrogen/acetonitrile pressure in LPCVD were 1000 °C and 100 Pa, respectively. The growth time was 1 h, and the furnace was cooled to room temperature with non-stop gas flow.

2.2. Transfer of NGr films

A protective PMMA (dissolved in anisole with a concentration 8%) layer was spin-coated on one

side of the as grown graphene films on copper. After heating at 90 °C for 5 min on a hot plate, the other side of the copper was exposed to O₃ plasma for 60s to remove the unnecessary graphene, and the sandwich structure was obtained. After that, the 1 M FeCl₃ was used to etch the Cu foils, resulting in a PMMA/graphene film floating on the surface of the solution (figure S1, supplementary section (stacks.iop.org/TDM/7/015002/mmedia)) [41, 42]. HCl and deionized water were used to wash the PMMA/graphene film several times, which was then transferred to ITO glass. After air drying, the PMMA film was removed by acetone, and then the substrate with graphene was rinsed with isopropyl alcohol and finally blow dried with N₂ gas. PMMA is an organic substrate that can be oxidized by photogenerated holes in photocatalytic reactions while ITO glass is a transparent, inorganic substrate that is typically unaffected by organic photochemical reactions; this motivated us to perform the substrate transfer.

2.3. Synthesis of silver nanoparticles

Silver nanocubes were synthesized by a polyol synthesis process reported earlier [43, 44]. Silver nitrate (AgNO₃) was the Ag precursor in this synthesis process. Na₂S and poly(vinyl pyrrolidone) (PVP) were used as the reducing and capping agents respectively. Briefly ethylene glycol (EG) was first heated up to 160 °C followed by addition of AgNO₃, PVP and Na₂S into the reaction medium. After a few minutes, the color of the solution turned to ruddy-brown which indicated the formation of Ag nanocubes. The size of the nanocubes was controlled by changing the duration of the reaction. The reaction time used in this study was seven minutes. It is to be noted that, Ag precursor and Na₂S in the solution will form Ag₂S at the initial stage of the reaction, but later this Ag₂S acts as both the seed and the reduction catalyst to form Ag nanocubes [44].

2.4. Physicochemical characterization

Field emission scanning electron microscopy (FESEM) was employed to characterize the surface morphological features of Ag nanoparticle coated N-doped graphene. A Zeiss Sigma FESEM with an accelerating voltage of 5 kV was used for this purpose. The fine structural and elemental analysis of lab-grown Ag nanoparticles were performed using a JEOL 2200 FS transmission electron microscope (TEM) equipped with a field emission gun. The accelerating voltage was 200 kV. Scanning TEM (STEM) mode with a nominal probe size of 1 nm was employed for the EDX mapping. An ultra-dilute solution of Ag nanoparticles was cast onto lacey carbon-coated copper TEM grids followed by drying under a solar simulator. Gatan micrograph was used to process the HRTEM (high resolution TEM) files (.dm3) and obtain lattice spacings. In order to reveal the crystalline properties of the plasmonic Ag nanoparticles, we used a Bruker D8 advance x-ray

diffractometer (XRD) equipped with a 2D detector (VANTEC-500). The x-ray radiation source was CuK α , $I_{\mu}S_{\mu}$ ($\lambda = 1.5406 \text{ \AA}$) operating at 50 W at room temperature. The vibrational properties of pristine N-doped graphene and Ag coated N-doped graphene were studied using a Raman spectrometer (Nd:YAG laser Raman Microscope, Nicolet Omega XR). The excitation wavelength of the Raman laser was 532 nm; the incident power was 10 mW and a 50X objective was employed. Diffuse reflectance spectra (DRS) for pristine N-doped graphene and Ag coated N-doped graphene, and absorption spectra (transmission mode) of pristine Ag nanoparticles in aqueous solution were collected using a Perkin Elmer Lambda-1050 UV-vis-NIR spectrophotometer equipped with an integrating sphere accessory.

The surface chemical attributes and elemental binding energies (BE) of N-doped graphene (NGr) and Ag decorated NGr were determined using x-ray photoelectron spectroscopy (XPS) acquired on a XPS (Axis-Ultra, Kratos Analytical) instrument equipped with a monochromatic Al-K α source (15 kV, 50 W) and photon energy of 1486.7 eV under ultrahigh vacuum ($\sim 10^{-8}$ Torr). The binding energy of adventitious carbon's C1s peak (BE ≈ 284.8 eV) was used as a standard to assign the BE of other elements. The obtained raw data (.vms files) was deconvoluted into various peak components using CasaXPS and the extracted data was plotted using Origin 2018. Ultraviolet photoemission spectroscopy (UPS) was performed to acquire work function and valence band spectra of materials using a 21.21 eV He lamp source. The surface topographical features of the transferred NGr from Cu surface to glass were acquired with an atomic force microscope (Bruker Dimension Edge) operating in air using tapping mode. A silicon AFM probe (TAP300-G-50) with resonant frequency 300 kHz and force constant 40 N m⁻¹ was used in this characterization. Kelvin probe force microscopy (KPFM) was used to measure the surface potential of the samples under investigation. A Dimension Fast Scan Atomic Force Microscope (Bruker Nanoscience Division, Santa Barbara, CA, USA) was employed for this purpose. A diode laser (425 nm) was used to perform KPFM measurements under illumination, in addition to measurements in the dark. Conducting copper tape was used to ground the samples with the AFM chuck prior to data collection. A SCM-PIT cantilever with 4.4 N m⁻¹ stiffness was used in this experiment. The relevant parameters associated with this experiment are a cantilever lift height of 75 nm, operating at 2 kHz lock-in bandwidth while maintaining a scan speed of 1 Hz. Tip bias was set to zero as a reference. Prior to each repetitive data collection step under light and in dark, a minimum of 5 min wait-time was used to ensure carrier transport equilibrium. The platinum tip work function was calibrated by measuring the contact potential difference of HOPG and the tip.

2.5. Measurement of surface photocatalytic transformation of 4-NBT to DMAB

A dilute aqueous solution of lab-grown Ag nanoparticles was spin-cast at 1000 rpm onto ITO/N-doped graphene surface and ITO glass substrates followed by 30 min of baking at 100 °C on a hot plate. Prior to the Raman stimulated surface catalytic experiments, an ultra-dilute solution of 4-NBT (5×10^{-5} M) in methanol was cast onto the ITO/N-graphene/Ag, ITO glass/Ag and bare ITO/N-graphene samples followed by vacuum drying at 60 °C. The excitation wavelength of the Raman laser was 532 nm and 633 nm with variable power from 0.1 mW to 10 mW. The other experimentally relevant parameters were a fluorescence correction factor of 4, aperture size of 50 μm pinhole, 2 μm spot size, a $10 \times$ objective, and $2 \text{ cm}^{-1}/\text{CCD}$ pixel element 900 lines mm^{-1} spectral dispersion grating. The Raman spectrum of DMAB was digitized from previously reported work [45]. Raman spectra were accumulated for 5×20 s exposure time in air at room temperature.

3. Optical simulations

Optical properties of the nanocube structures were investigated using Lumerical FDTD (finite difference time domain) simulation software. The smoothed and rounded nanocube structures were simulated with reference to the experimental SEM and TEM images obtained, and spanned edge lengths of 45 nm with a radius of curvature of 17 nm. The simulated nitrogen-doped graphene substrate was 30 nm thick. The simulations were performed for various combinations of dimer nanocube structures where the nanocubes were placed at a distance of 34 nm from each other or were in physical contact with each, both in the presence and the absence of the nitrogen-doped graphene substrate. The simulations were exclusively performed in vacuum. Scattering and absorption cross sections, and electric field intensity profiles at the wavelength of 532 nm were captured using near-field and far-field profile and frequency monitors. Optical constants for nitrogen-doped graphene were obtained from the work of Shen *et al* [46], who calculated the refractive index of nitrogen-doped graphene thin films using spectroscopic ellipsometry. A light source of bandwidth range 200–800 nm was incident upon the structures at a normal angle from above. Lumerical's in-built refractive index monitor was utilized to confirm that the structures were appropriately configured and modeled throughout the course of the simulation. PML absorbing boundary conditions were utilized for the simulation, allowing for the absorption of light waves (both propagating and evanescent) with minimal reflections. The relevant results pertaining to the electric field intensity profiles were obtained at the wavelength of 532 nm as viewed along different planes, such as xy , xz , and yz planes.

4. Results and discussion

4.1. Physicochemical properties

The field emission scanning electron microscopic (FESEM) image of pristine N-doped graphene and with synthesized Ag nanoparticles on its surface are shown in figures 1(a)–(c). The low magnification image shows some white patches (figure 1(a)) and a closer view (figure 1(b)) reveals the wrinkles of 2D nanosheets, which is a general topological feature for graphene and N-doped graphene [15, 19]. The monolayer of Ag nanoparticles (figure 1(c)) was dried on a hot plate at 100 °C before casting the 4-NBT solution on it. This dense distribution of Ag nanoparticles on N-doped graphene substrate is expected to enhance the local electromagnetic field desired for SERS (surface enhanced Raman spectroscopy) experiments [47]. Figure 1(d) shows the transmission electron microscopic image of these Ag nanoparticles on a TEM copper grid. The size and shape of these lab-synthesized particles were determined from these images. They have an intermediate structural shape between a cube and sphere, in other words cubes with rounded corners. In order to determine the fine structural features, we collected high resolution TEM (HRTEM). Figures 1(e) and (f) show the HRTEM images of Ag nanoparticles. The obtained lattice spacing, d has a value of 0.24 nm which is associated with (1 1 1) crystal plane of Ag and is in good agreement with x-ray diffraction peak shown in figure 2(a) [48, 49]. All the XRD peaks in figure 2(a) are indexed to face-centered-cubic silver [48, 49]. We also opted for the elemental analysis of home-grown Ag nanoparticles. Figures 1(g)–(i) show the presence of Ag with negligible amount of oxygen in the EDX mappings collected in STEM mode. Thus, the lab-synthesized Ag nanoparticles have high crystallinity and compositional features desirable for harnessing plasmonic properties in solar energy harvesting applications.

Raman spectroscopy is a convenient and powerful technique to determine crystallite size, number of layers, doping and disorder in graphene and other carbon-based materials [4, 7]. The Raman spectral features (532 nm excitation) of N-doped graphene and composite systems with Ag nanoparticles are presented in figures 2(b) and (c). The D, G and 2D are the important and prominent bands for analyzing graphene and graphene-based derivatives. The first order Raman scattering process that gives rise to doubly degenerate E_{2g} phonons at the Brillouin zone, constitutes the G band, whereas the D and 2D bands are the results of a zone-boundary phonon induced second order, double-resonance process [7, 50]. The external doping breaks the translational symmetry of graphene and the D band represents doping induced defects in graphene-based materials [51]. In our pristine N-doped graphene samples, we found two distinct regions, one with a high intensity ratio of the D and G bands I_D/I_G ,

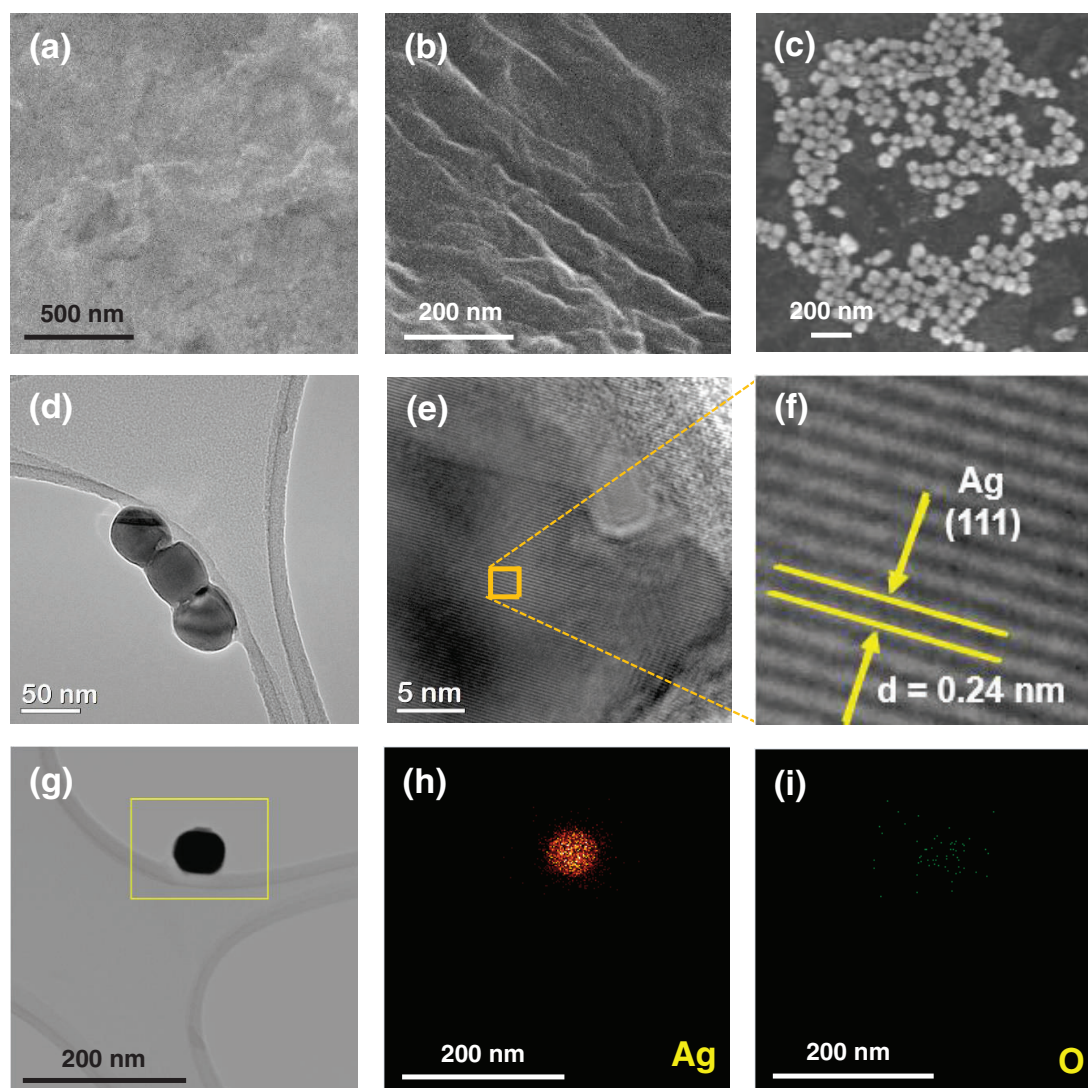


Figure 1. (a) and (b) FESEM image of N-doped graphene on glass at low and high magnification respectively (c) FESEM image of a monolayer of Ag nanoparticles on N-doped graphene (d) TEM image of Ag nanoparticles (e) HRTEM image of Ag nanoparticle (f) selected magnified region of figure (e) for identifying crystal plane (1 1 1) (g) bright field STEM image of a lone Ag nanoparticle and (h)–(i) STEM elemental mapping for (h) silver and (i) oxygen.

and the other one with low I_D/I_G . This nonuniformity in the peak intensity ratio I_D/I_G , is a consequence of inhomogeneous doping of nitrogen in graphene and has been observed in many earlier reports [50]. This peak intensity ratio is proportional to defects and is inversely proportional to crystallite size [51]. Therefore I_D/I_G is also proportional to N-doping level as reported earlier [52]. Figure 2(b) represents high I_D/I_G , corresponding to high doping, high defects and smaller crystallite size and figure 2(c) depicts low doping, low defects and larger crystallite size as it has a lower I_D/I_G . N-doping induced reduction in crystallite size is consistent with previous works [52]. The intensity ratio I_G/I_{2D} is a measure of the thickness of graphene or the number of atomic layers [53]. The higher value of I_G/I_{2D} in figure 2(c) (pristine NGr) compared to that in figure 2(b) supports the crystallite size comparison as well. However, we found suppressed 2D bands for both kinds of regions in N-doped graphene/Ag hybrid (insets of figures 2(b) and (c)), which indicates that

two zone-boundary phonons mediated intervalley double resonance scattering around the K-point of the Brillouin zone [50] is largely inhibited in the composite system. The reduction in peak intensity ratio I_{2D}/I_G is an indication of higher electron concentration [54, 55]. This is expected, since the Ag surface plasmon decay generated hot electron injection into graphene, can potentially increase electron concentration, resulting in reduction of I_{2D}/I_G . Plasmon induced charge carrier enhancement can occur through other possible mechanisms as well. This is discussed later in this article. The absorption spectra of pristine N-doped graphene and N-doped graphene/Ag composites on glass are presented in figure 2(d) (main). The inset shows the absorption spectra of pristine Ag nanoparticles in aqueous solution and on glass. The plasmonic peaks for the N-doped graphene/Ag composites and pristine Ag nanoparticles on glass are relatively broad compared to the absorption peak of pristine Ag nanoparticle in aqueous solution, possibly due to an enhanced

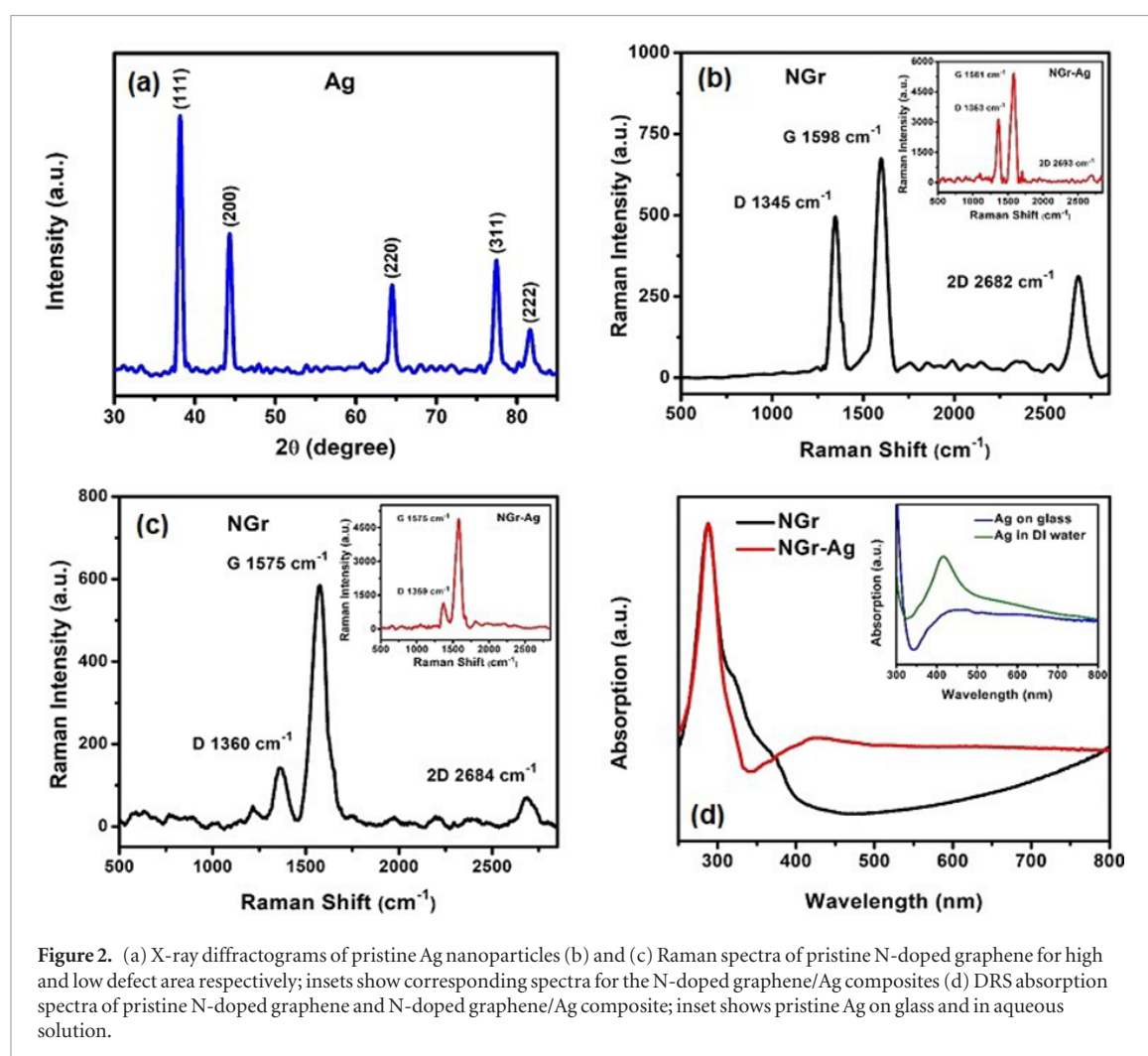


Figure 2. (a) X-ray diffractograms of pristine Ag nanoparticles (b) and (c) Raman spectra of pristine N-doped graphene for high and low defect area respectively; insets show corresponding spectra for the N-doped graphene/Ag composites (d) DRS absorption spectra of pristine N-doped graphene and N-doped graphene/Ag composite; inset shows pristine Ag on glass and in aqueous solution.

aggregation of Ag particles on glass and graphene/glass substrate [56]. The main absorption peak of Ag nanoparticles is sensitive to the size and shape of the Ag nanoparticles. The position of this peak at ~ 425 nm for the synthesized Ag nanoparticles, is consistent with previously reported data [43, 56]. The enhanced absorption in the NGr/Ag hybrid is a general feature of exciton-plasmon coupled systems [32].

XPS was used to determine the surface and sub-surface (up to ~ 10 nm) chemical composition of NGr and NGr-Ag. The elemental survey scan (figure 3) using XPS of NGr displayed all the low energy and deep core level features corresponding to C1s, N1s, O1s, OKLL peaks. The N atom doping level was found to be 3.17 at%. For NGr-Ag, all the relevant peaks of NGr were observed along with additional peaks of Ag3d, Ag4s and Ag4p confirming the presence of Ag nanoparticles on the surface of N-doped graphene. High resolution core-level XPS spectra of NGr in C1s region exhibited an intense peak at BE ≈ 285.11 eV with shoulder peak in the high BE region (figure 4(a)). The C1s peak can be deconvoluted into four well-separated chemically shifted peak components centered at BE ≈ 285.11 , 286.34, 287.15 and 288.86 eV. The peaks at BE ≈ 285.11 and 286.34 eV originated due to sp^2 hybridized carbon that compose the graphene skel-

eton (Csp^2-C) and sp^2 carbons bonded with graphitic, pyridinic and pyrrolic nitrogens (Csp^2-N) while peaks at 287.15 and 288.86 eV were assigned to Csp^3-N and $C=O/N-C=O$ species of carbon [57–60].

The high resolution N1s spectrum of NGr can be deconvoluted into three peak components located at 399.29, 400.25 and 401.56 eV, corresponding to pyridinic, pyrrolic and graphitic nitrogen atoms present in N doped graphene, respectively (figure 4(b)) [61–63]. The deconvoluted spectra of NGr in O1s region showed three peak components at 530.00, 531.76 and 533.98 eV, attributed to C–O, C=O and surface adsorbed oxygens ($-OH/O_{ads}$) respectively (figure 4(c)) [15, 64]. After drop casting Ag nanoparticles on the NGr (NGr-Ag), the peak position for all elements was almost identical to pristine NGr, demonstrating that the chemical structure of NGr is preserved after the decoration of AgNPs (figures 4(a)–(c)). Further, the presence of two well resolved XPS peaks at 368.33 and 374.28 eV in Ag3d region of NGr-Ag confirms the presence of Ag (0) nanoparticles (figure 4(d)) [65, 66].

Defect-free pristine graphene is metallic in nature with a theoretical zero-bandgap. However, the introduction of N atoms into a graphenic framework followed by bonding with adjacent sp^2 hybridized carbons modifies the charge distribution over neigh-

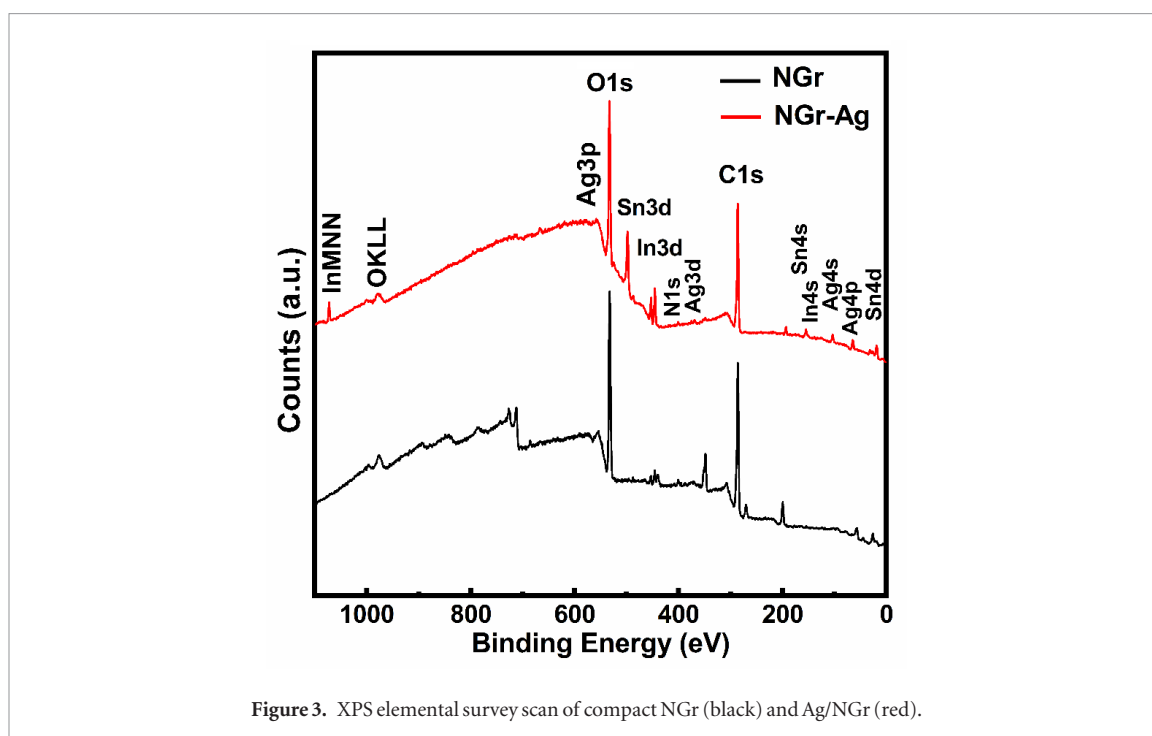


Figure 3. XPS elemental survey scan of compact NGr (black) and Ag/NGr (red).

boring carbon atoms. Additionally, the orbital overlap of sp^2 hybridized graphitic nitrogen bonded to three sp^2 carbons releases two extra electrons into the π conjugated aromatic system which increases the electron density on the surface of NGr, which in turn breaks the symmetry of the graphene sub-lattice and results in the shifting of the Fermi level above the Dirac point and a band gap is created between the valence and conduction band [5, 7, 10, 67]. However, slightly contrary of the above picture, Kondo *et al* [68] and Schiros *et al* [69] reported experimental reports combined with first principle calculations that showed the effect of bond types on carrier concentration. Nitrogen doped graphene containing graphitic N, acts as a n-type semiconductor, due to charge transfer from N dopant atom to neighboring C atoms and pyridinic N containing graphene behaves like a p-type semiconductor [68, 69]. From figure 4(b), the chemical shifts of N1s BE to positive (401.56 eV) and negative (399.29 eV) values agree well with the negatively and positively charged N atoms of graphitic and pyridinic structures respectively.

The electronic band structures of NGr and NGr-Ag materials were determined from the ultraviolet photoelectron spectra (UPS) (figures 5(a) and (d)). The expression $WF(\phi) = 21.21 - E_{\text{cut-off}}$ was used to estimate the value of WF where 21.21 eV is the energy of the incident, He I laser light, and $E_{\text{cut-off}}$ is the cut-off energy of secondary electrons. The extrapolation of the linear region of the graph to the vertical and horizontal axes gave the value of cut-off energy of secondary electrons $E_{\text{cut-off}}$ at the point of intersection. The $E_{\text{cut-off}}$ values for compact NGr and NGr-Ag were calculated to be 17.74 and 17.49 eV, and corresponded to work function (ϕ) values of 3.47 and 3.72 eV respectively (figure 5(a) and inset). The slight increase in the

WF energy after addition of Ag nanoparticles demonstrates downshifting of the Fermi level which indicates transfer of negative charge from N-doped graphene sheets to Ag. Further, the positions of the valence band maxima obtained from the intersection point of the extrapolated linear region of the graph for NGr and NGr-Ag were found to be 0.26 and 0.17 eV, respectively (figure 5(b)). Keeping in mind that the Fermi level lies close to the conduction band edge for a n-type semiconductor, the obtained VB maxima can be regarded as bandgap values. The obtained bandgap value for NGr was consistent with previous literature values reported for approximately similar N doping (2.9 at%) [52]. Further, a smaller energetic separation between the VB maximum and the Fermi level after Ag decoration in NGr-Ag indicated a reduced n-type character and thus complied with WF values demonstrating a downshift of Fermi level due to electron transfer from N-doped graphene to Ag.

Figure 6(a) shows the AFM height image of N-doped graphene nanosheets on glass after being transferred from copper. A thick layer of NGr nanosheets can be visible in the image. The transfer process of CVD-grown NGr generally induces wrinkles on the graphene surface (figure 1). There exist some thick patches of nanosheets of NGr in the FESEM images as mentioned earlier in this section. The inset of figure 6(a) shows the corresponding line cross-section of the height image of this thick wrinkled area. The line scan shows an average height of ~ 34 nm of NGr nanosheets. Thick layers are not very useful for electronic device applications such as transistor channels, but for photocatalysis a large thickness is not detrimental. Surface potential, which is defined as the contact potential difference between KPFM tip and the material surface has been measured in dark and under

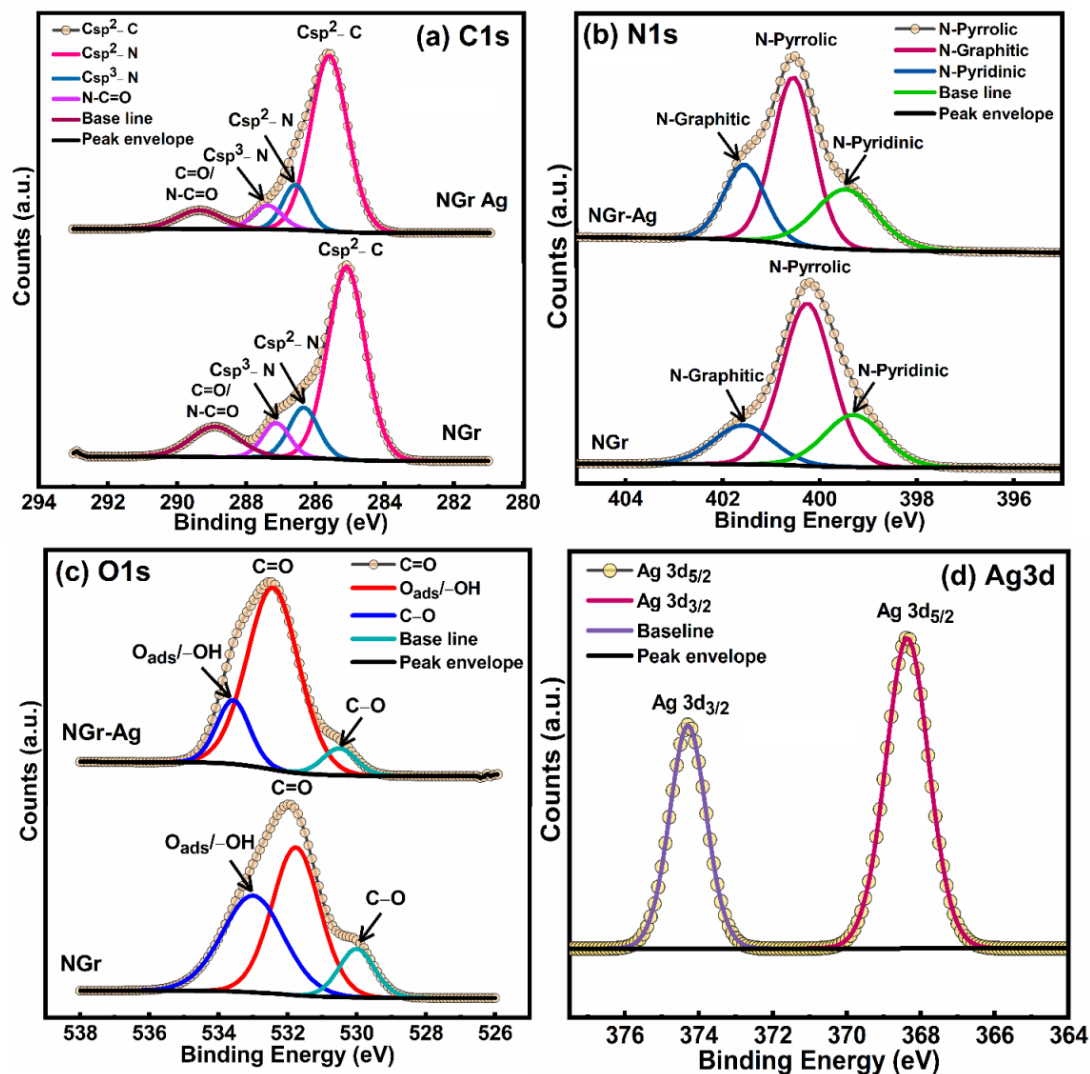


Figure 4. HR-XPS core level spectra of compact NGr and NGr-Ag in (a) C1s region, (b) N1s region, (c) O1s region and HR-XPS of NGr-Ag in (d) Ag3d region.

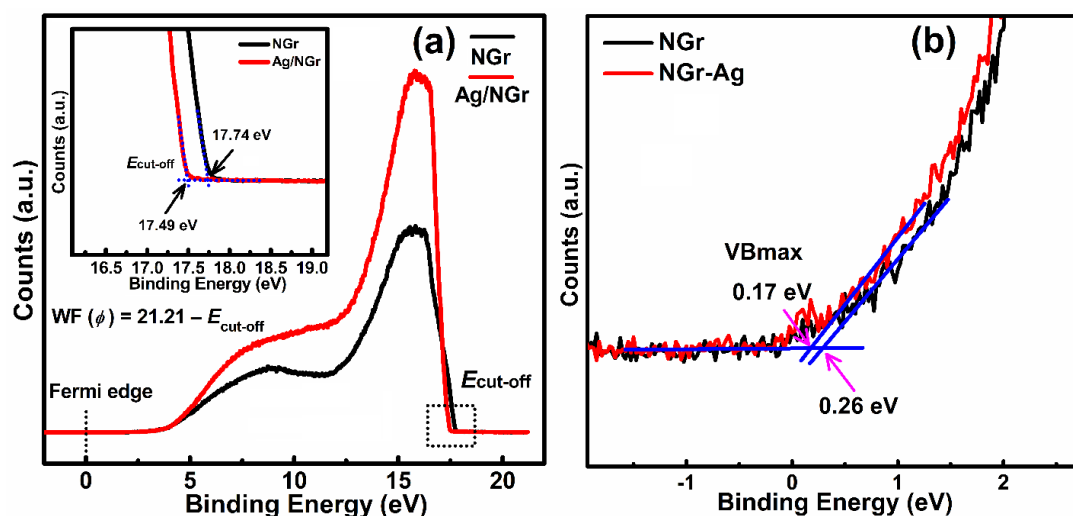


Figure 5. (a) UPS work function spectra of NGr and NGr-Ag. Inset shows cut-off energy ($E_{cut-off}$) of the secondary electron and (b) UPS valence band spectra showing the position of valence band edge (VBmax) below the Fermi level.

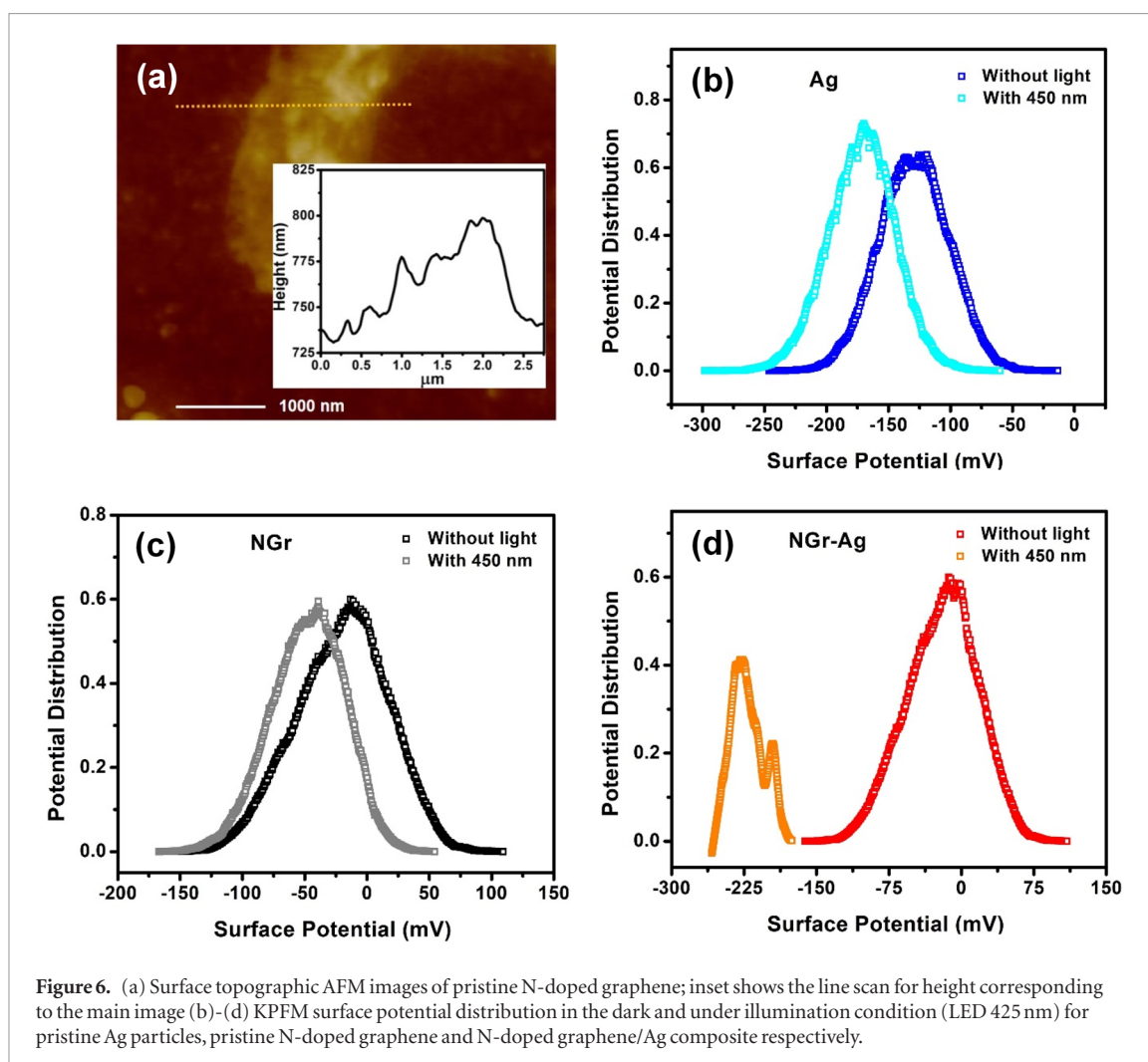
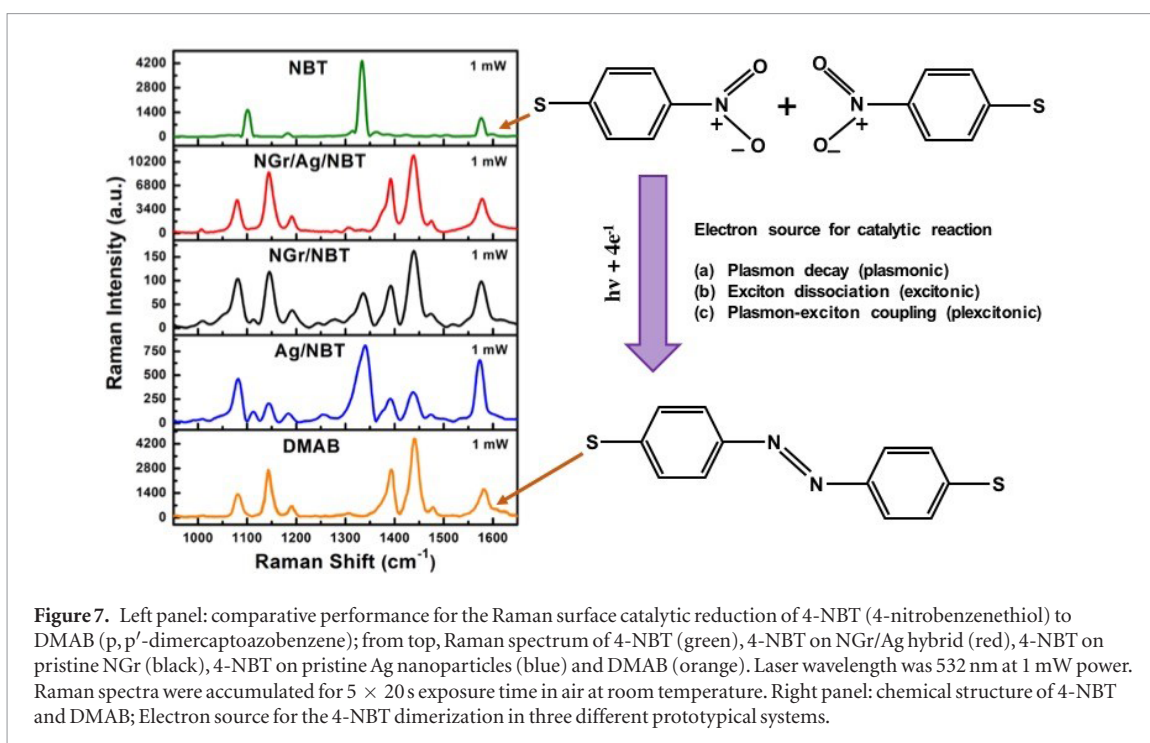


Figure 6. (a) Surface topographic AFM images of pristine N-doped graphene; inset shows the line scan for height corresponding to the main image (b)–(d) KPFM surface potential distribution in the dark and under illumination condition (LED 425 nm) for pristine Ag particles, pristine N-doped graphene and N-doped graphene/Ag composite respectively.

illumination. KPFM is a powerful technique to elucidate the nature of charge carrier dynamics [70–72]. The charge carrier photogeneration in the photocatalyst can be imaged by this microscopic method. We have obtained the comparative photoresponse of all three systems, namely plasmonic, excitonic and plexcitonic, comprising bare Ag, bare NGr and NGr/Ag hybrid respectively. Figures 6(b)–(d) show the surface potential distribution of pristine Ag nanoparticles, pristine NGr and NGr/Ag hybrid in the dark and under light illumination (425 nm) obtained using KPFM. Illumination produces photogenerated charge carriers whose redistribution causes the shifting of work functions for the systems under study, thus changing the surface potentials. Different light induced carrier enhancement mechanisms in bare Ag, bare NGr, and NGr/Ag composite occur, such as plasmon induced electric field amplification followed by accumulation of charge carriers, optical transition leading to formation of excitons and coupling of plasmon–exciton respectively. Therefore, the surface potential difference between dark and illumination conditions is a measure of the photoresponse of the surface. From figures 6(b)–(d), it is evident that NGr/Ag hybrid system shows the highest photoresponse, resulting in a large negative shift of surface potential, compared to the

other two systems, pristine Ag and pristine NGr. This is reminiscent of the significant reduction of Raman peak intensity ratio I_{2D}/I_G for the hybrid system, as a result of huge charge carrier accumulation discussed earlier. A correlation between plasmon induced local field enhancement and surface potential change has also been reported in GaN and Ag nanoparticle hybrid, where a concomitant reduction in surface potential was observed with optical field enhancement [73].

The wavelength corresponding to the illumination used during photo-KPFM measurements (450 nm) was deliberately chosen to be close to the LSPR peak of the rounded Ag nanocubes (425 nm, see figure 2(d) and inset). The bare Ag particles exhibit a mere -100 mV shift in surface potential upon illumination. Bare NGr shows a small shift in surface potential of ~ -40 mV upon illumination. However, NGr decorated with Ag nanocubes shows a large shift of -225 mV upon illumination, which is indicative of long-lived charge separation in the NGr/Ag hybrid. Considering the ground state charge transfer in the NGr/Ag system indicated by UPS data (figure 5) and the proximity of the illumination wavelength to the LSPR of Ag nanocubes, the most likely mechanism for extended charge separation is efficient injection of hot electrons from Ag into NGr following the decay of the Ag surface plas-



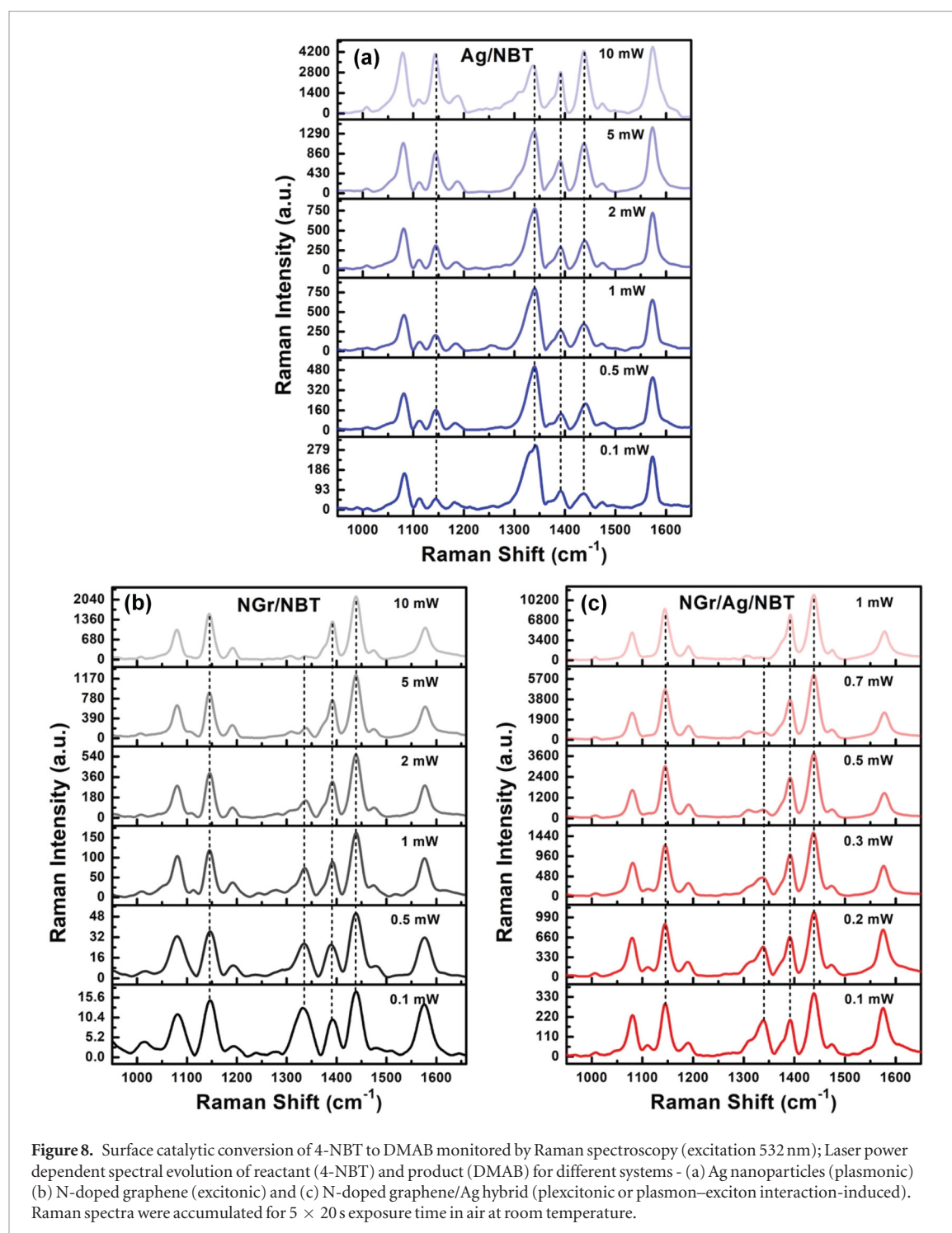
mons. We surmise that ultrafast chemical interface damping of the Ag surface plasmon may be responsible for the clear accumulation of electrons in NGr and long-lived charge separation. This is because the sequential mechanism consisting Landau damping of the plasmon followed by hot electron injection is known to exhibit much poorer charge separation and higher losses due to much faster competing thermalization processes involving electron–electron scattering and hot electron–phonon collisions [31].

4.2. Surface photocatalytic transformation of 4-NBT to DMAB

In this work, we have investigated a comparative performance analysis of surface catalytic reactions for converting 4-NBT to DMAB using three systems, pristine Ag nanoparticles, pristine N-doped graphene and N-doped graphene/Ag composite. These systems represent three distinct mechanisms of photocatalysis with different charge carrier dynamics, such as plasmonic, excitonic and plexcitonic (coupled plasmon and exciton) respectively. The photoconversion or dimerization of 4-NBT to DMAB is a reduction reaction that involves four electrons (figure 7) [27, 74]. Surface plasmon decay generated hot electrons in plasmonic metals are injected into 4-NBT with high kinetic energy, and are responsible for performing this reduction [27, 30]. A large kinetic energy is required to overcome the potential barrier and complete the reduction reaction. It is worth mentioning that surface plasmon driven oxidation reaction involves a completely different mechanism. It can be performed either by a hot hole generated by plasmon decay or by the plasmonic hot electron driven transformation of singlet oxygen into triplet oxygen, where triplet oxygen plays the role of the

catalyst [75, 76]. The excitonic reduction of 4-NBT to DMAB has been observed on Cu_2O surfaces [45]. The photogenerated electrons and holes in the conduction and valence bands respectively under light illumination, perform the catalytic reduction and oxidation for any excitonic photocatalyst, constrained by the energy requirements of electrons and holes with respect to reduction and oxidation potentials of the reactions. Apart from pure plasmonic and pure excitonic photocatalysis, plexcitonic or plasmon–exciton co-driven photocatalysis has the immense potential to drive these surface catalytic reactions as the exciton–plasmon interaction increases the plasmon to electron conversion efficiency, as well as prolongs the hot electron lifetime [26, 28, 29, 77].

Figure 7 shows the Raman spectra (excitation wavelength 532 nm) of 4-NBT and DMAB. The Raman peaks at 1101, 1332 and 1576 cm^{-1} of 4-NBT are assigned to S–C stretching vibration, $\nu_s(\text{NO}_2)$ vibration and C = C stretching vibration of benzyl ring respectively [27, 78]. DMAB Raman peaks are identified at 1142, 1392 and 1439 cm^{-1} . The band at 1142 cm^{-1} is attributed to C–N stretching vibration, and the peaks at 1392 and 1439 cm^{-1} arise due to ag_{16} and ag_{17} vibrational modes respectively, related to N = N stretching [27, 79]. The comparative surface catalytic efficiencies, at a constant laser power of 1 mW, are presented in figure 7. The surface catalytic reduction of 4-NBT to DMAB is highest for the NGr/Ag hybrid system as evidenced by the complete disappearance of the $\nu_s(\text{NO}_2)$ vibration of 4-NBT at 1332 cm^{-1} , followed by pristine NGr and pristine Ag respectively. Figure 8 shows the laser power dependent gradual evolution of DMAB peaks for these three systems. In all the three systems gradual decrease of main 4-NBT peaks (1332 cm^{-1}) and a simultaneous gradual



increase of the DMAB peaks mentioned earlier, occurs with increasing laser power. We can quantitatively compare the 4-NBT reduction efficiency for the three different systems. The main Raman peaks for 4-NBT and DMAB are at 1332 cm^{-1} and 1439 cm^{-1} respectively. Figure S3 (supplementary section) shows the intensity ratios of these peaks for 4-NBT and DMAB ($I_{\text{NBT}}/I_{\text{DMAB}}$) versus laser power (excitation wavelength 532 nm). At a laser power of 1 mW, the peak intensity ratios, $I_{\text{NBT}}/I_{\text{DMAB}}$, are 2.32, 0.45 and 0.04 for Ag, NGr and NGr-Ag systems respectively. From this plot it is evident that the NGr-Ag plexcitonic system has the highest photocatalytic efficiency, while pristine NGr

also shows a remarkable superiority in reduction reactions over stand-alone Ag nanoparticles. From figure 8 it is evident that the surface plasmons in Ag nanoparticle alone cannot completely transform 4-NBT into DMAB even at a laser power as high as 10 mW. Notice that in this experiment we used $10 \times$ objective for all three systems, which gives much lower intensity compared to $50 \times$ or $100 \times$. Pristine graphene completed this chemical transformation at 10 mW power, while NGr/Ag hybrid catalyst required only 1 mW. These results demonstrate that pristine N-doped graphene alone can drive the surface catalytic reduction reaction without any plasmonic co-catalyst. The Raman spec-

tral intensity at higher laser power of 4-NBT/DMAB on NGr surface is also comparable to that of pristine Ag supported system, but indeed much weaker than the hybrid system NGr/Ag. This implies that NGr has potential for SERS applications for system where it does not have any reactivity with adsorbed molecule, in other words where it is expected to behave noninvasively. Unlike graphene-Ag nanowire system reported earlier [26], we have observed the DMAB peak at 1142 cm^{-1} in both the excitonic N-doped graphene and plexcitonic NGr/Ag systems. Metal-semiconductor hybrids have been thoroughly explored in the recent past as these hybrid systems combine two systems possessing complementary optical properties. Fundamental optical excitations in metal are surface plasmons that are collective oscillations of conduction band electrons, while in semiconductor these are excitons or bound electron-hole pairs which are the product of transitions between valence and conduction band energy levels [32]. The plasmonic metals have the potential to enhance optical field through concentrating electromagnetic energy and the semiconductors can generate and support long-lived excitations that are capable of harvesting solar energy [32]. NGr/Ag composite system promotes plasmon-exciton coupling that induces a strong amplification of the local electromagnetic field, produces accumulation of high-energy hot electrons following plasmon dephasing, and has high absorption cross-sections, thus demonstrating superior photocatalytic prowess. We have opted to investigate this surface photocatalytic activity using 633 nm laser in order to shed some additional light on the dominant reaction mechanism in different model systems. Figures S4–S6 (supplementary section) show the laser power dependent gradual evolution of DMAB peaks for these three systems. While almost similar comparative performance was observed, N-doped graphene showed a slight efficiency enhancement compared to that with 532 nm laser. The other two systems, Ag nanocubes and NGr/Ag hybrid demonstrated a reduced performance. These results are not unexpected as for the plasmonic Ag and plexcitonic NGr/Ag systems, resonance peaks (figure 2(d)) are further away from 633 nm laser compared to 532 nm laser. The minor enhanced performance for the excitonic NGr could be a consequence of a slightly higher absorption (figure 2(d)). The different possible plasmon-exciton coupling mechanisms are discussed later in this article.

4.3. Interaction with incident optical field

FDTD simulations were carried out to model the plasmonic and plexcitonic systems of the Ag nanoparticles in the absence and presence of NGr substrate respectively. The relevant physical features of Ag nanoparticles were obtained from SEM and TEM data. Different arrangements of Ag nanoparticles with and without NGr substrate have been studied as mentioned earlier. Figures 9 and S12 (supplementary

information) show the electric field distribution for two Ag nanoparticles in the absence and presence of NGr substrate for two arrangements, separated by 34 nm and in physical contact. The k vector and E -field polarization direction were along z and x directions respectively. In both systems, the E -field intensity is highly amplified between the Ag particles and between NGr and Ag. Similar local field enhancement can be observed in figures S11 and S13 as well, where these two systems are exactly same as figures 9 and S12, except for the E -field polarization direction, which is now y . The maximum field is concentrated between NGr and Ag particles (in the vicinity of the interface) for all four systems (figures 9(d), S11(d), S12(d) and S13(d)). This SPR induced local field enhancement has the immense potential to enhance electron concentration in NGr through various mechanisms that are discussed later in section 6. The reduction of E -field intensity in the regions where Ag nanoparticles are in direct contact with NGr (figures 9(d), S11(d), S12(d) and S13(d)) is indicative of plasmon induced energy transfer from Ag into NGr. Figures (S7)–(S10) show simulated absorption and scattering results for these systems with E -field polarized in y direction only. The absorption peaks of isolated Ag nanoparticles without and with NGr substrate show a blue shift (figures S7 and S8) compared to the experimentally obtained data (figure 2(d)). However, when two Ag nanoparticles are in direct physical contact these peaks (figures S9 and S10) are redshifted. The spin-cast Ag nanoparticles on NGr have both systems present as evidenced from SEM (figure 1(c)). LSPR peaks are broadened on the NGr substrate relative to the isolated nanoparticles, similar to the experimental data. In all the plots (figures S7–S10) scattering is dominated by absorption, implying faster plasmon dephasing [80].

5. DFT Modeling of N-doped graphene

5.1. Computation and modeling details

The electronic properties of three different types of nitrogen doped graphene, namely graphitic, pyridinic and pyrrolic [8] were calculated and compared with pristine undoped graphene within the framework of density functional theory (DFT) [81] as implemented in the software package OpenMX 3.8 [82]. Spin polarization was considered in all the calculations using Perdew–Burke–Ernzerhof (PBE) exchange correlation functional with the general gradient approximation (GGA) [83]. Numerical pseudoatomic orbitals centered on atomic sites were used for the basis set. A periodic system with the supercell consisting of 192 carbon atoms were used for pristine graphene. Three single layers of graphene were vertically stacked in the z -direction. The N-doped graphene systems were also constructed in a similar way with the dopant N atoms residing in each of the three layers. Three systems were studied containing only one type of doping, either of graphitic N, pyridinic N and pyrrolic N, and the fourth

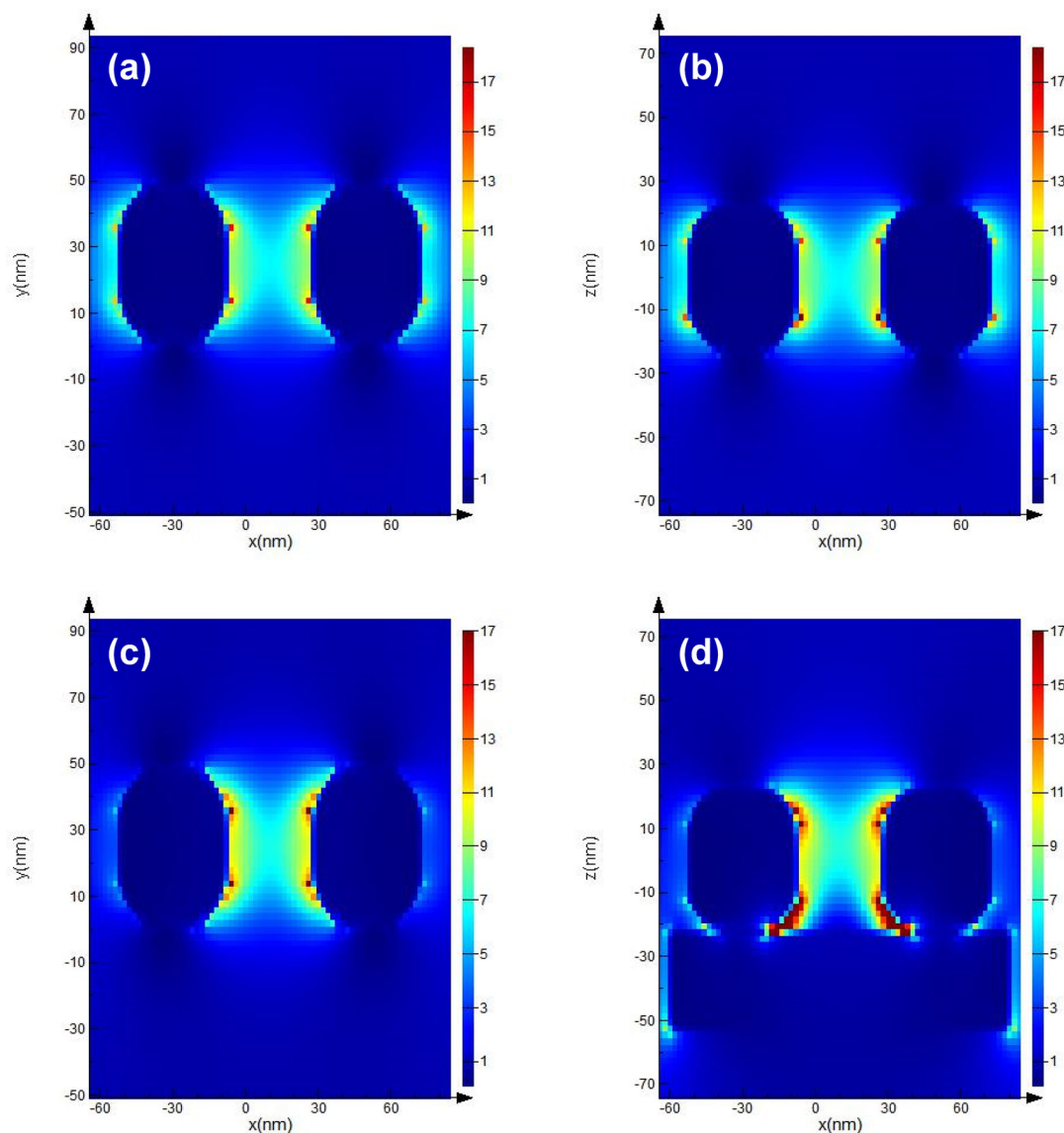


Figure 9. Electric field intensity distribution of two 34 nm apart Ag nanoparticles (cubes with rounded corners) at an incident wavelength of 532 nm; (a) in the xy plane without any substrate, (b) in the xz plane without any substrate, (c) in the xy plane with N-doped graphene substrate, and (d) in the xz plane with N-doped graphene substrate. The electric field component was x -polarized.

system comprised of all three types of dopants (figures 10 and S14). Figure 10(e) shows three types of dopant N-atoms as N1, N2 and N3 for graphitic, pyridinic and pyrrolic respectively. The ratio of N and C atoms was kept low, in order to be consistent with the XPS results, discussed earlier. Gaussian broadening method was used to study the projected density of states (PDOS) for the dopant N atoms, neighboring and the remote C atoms from the dopant atoms.

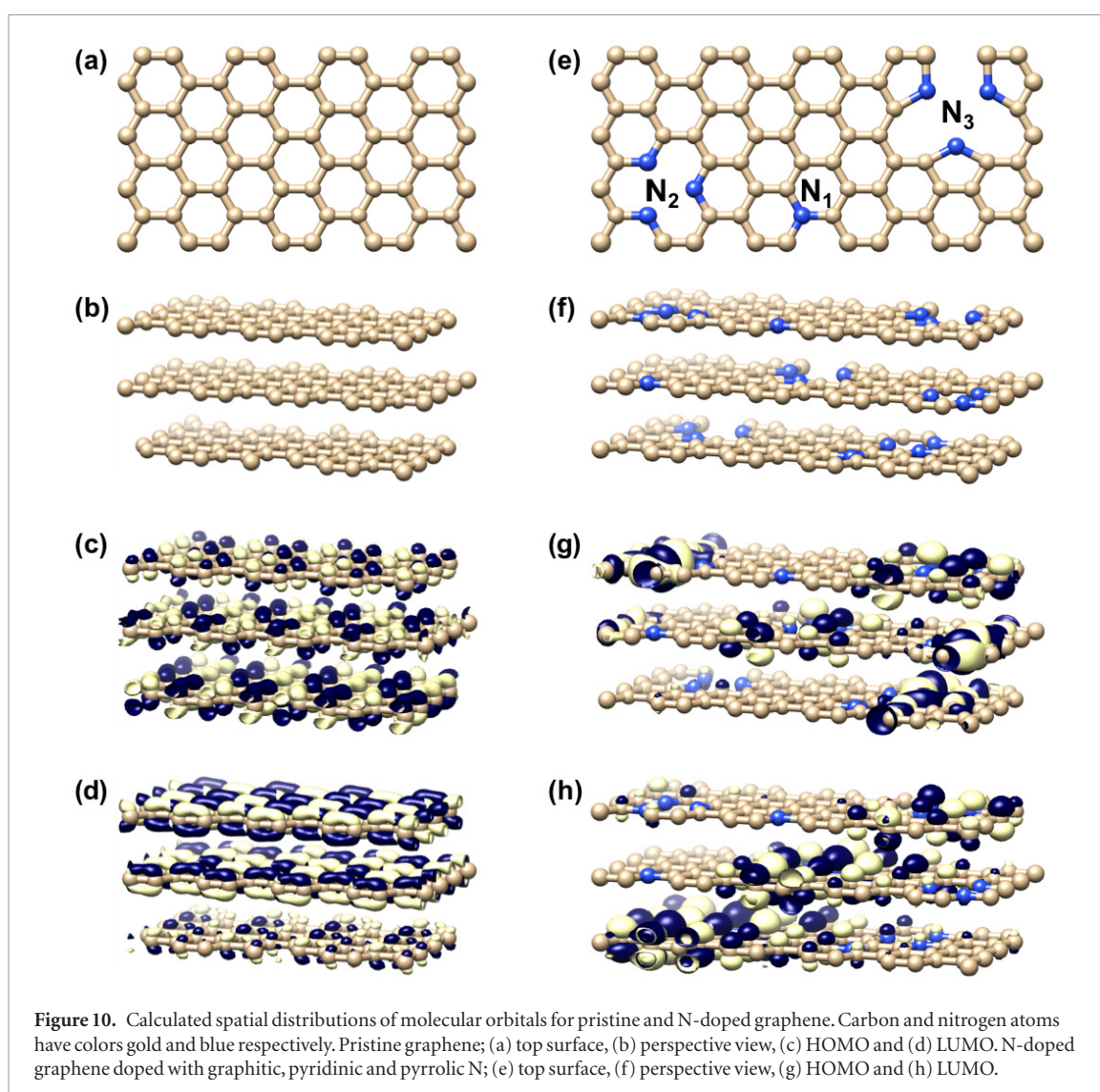
5.2. Results and analysis

Molecular orbital distribution and the PDOS of the optimized structures were plotted and analyzed in order to compare the electronic properties of the nitrogen doped and the pristine undoped graphene. Highest occupied molecular orbital (HOMO) and lowest unoccupied molecular orbital (LUMO) have been shown in figures 10 and S14 (supplementary

section). HOMO and LUMO are delocalized in pristine graphene, whereas N-doping introduces significant spatial localization of these molecular orbitals near the dopant sites, indicative of high chemical reactivity [84].

Pyrrolic and pyridinic systems have stronger localization compared to graphitic systems. These localization is a consequence of the introduction of an unpaired electron into graphenic framework upon N-doping [84].

PDOS have been plotted separately for sp^2 and p_z like states, of individual atomic sites in pristine and N-doped graphene. These plots are shown in figures 11 and S15 (supplementary section). For the N-doped systems PDOS at the dopant N atoms, neighboring and far-located C atoms have been selected. These results indicate that high number of states near the Fermi level (set at 0 eV) can be created at the dopant sites and the



neighboring C atoms compared to the remote C atom in the N-doped graphene and the pristine graphene. This implies chemical reactivity enhancement upon nitrogen doping. Figures 11 and S15 show that all three types of doping can enhance chemical reactivity of pristine graphene. Pyrrolic N and the neighboring C sites have highest reactivity, followed by pyridinic and graphitic systems respectively. Therefore, a correlation exist between molecular orbital localization and accumulation of states near the Fermi level. Thus, the dopant sites and the neighboring regions are expected to be the stronger sites for the surface catalytic reactions in NGr.

6. Mechanisms of photoreduction

Now, let us revisit the scenarios of photocatalytic reduction reactions for three different systems, namely plasmonic, excitonic and plexcitonic. When light falls on the Ag nanoparticles, it excites collective oscillations of conduction electrons, called plasmon. This surface plasmons are analogous to quantum harmonic oscillators, creating alternating regions of higher and lower electron densities [85]. Some of the

stored light quanta stored in plasmons are reemitted as light but most plasmons decay into electrons and holes. When incident photon frequency is in resonance with the natural frequency of the oscillating valence electrons on the metal surface (Ag nanoparticles), LSPR is excited [86]. Surface plasmons are coherent oscillations of electrons in space and energy. They have the potential to drive photocatalytic reactions through different mechanisms. The dephasing of this coherent oscillation can occur by different mechanisms, such as, elastic re-radiation of photons and nonradiative Landau damping that gives rise to the high energetic hot electrons and holes [86]. Hot electrons can perform the photocatalytic reduction reaction of 4-NBT to DMAB [27]. The ability of hot electrons generated by Landau damping to perform useful work is severely constrained by their short lifetime, since hot carriers in metals experience electron–electron scattering and electron–phonon collisions over femtosecond to picosecond timescales that cause their thermal equilibration [31]. There is another route of direct plasmonic photocatalysis for plasmonic metal nanoparticles when they are in contact with adsorbate molecules. In this mechanism, excited plasmonic

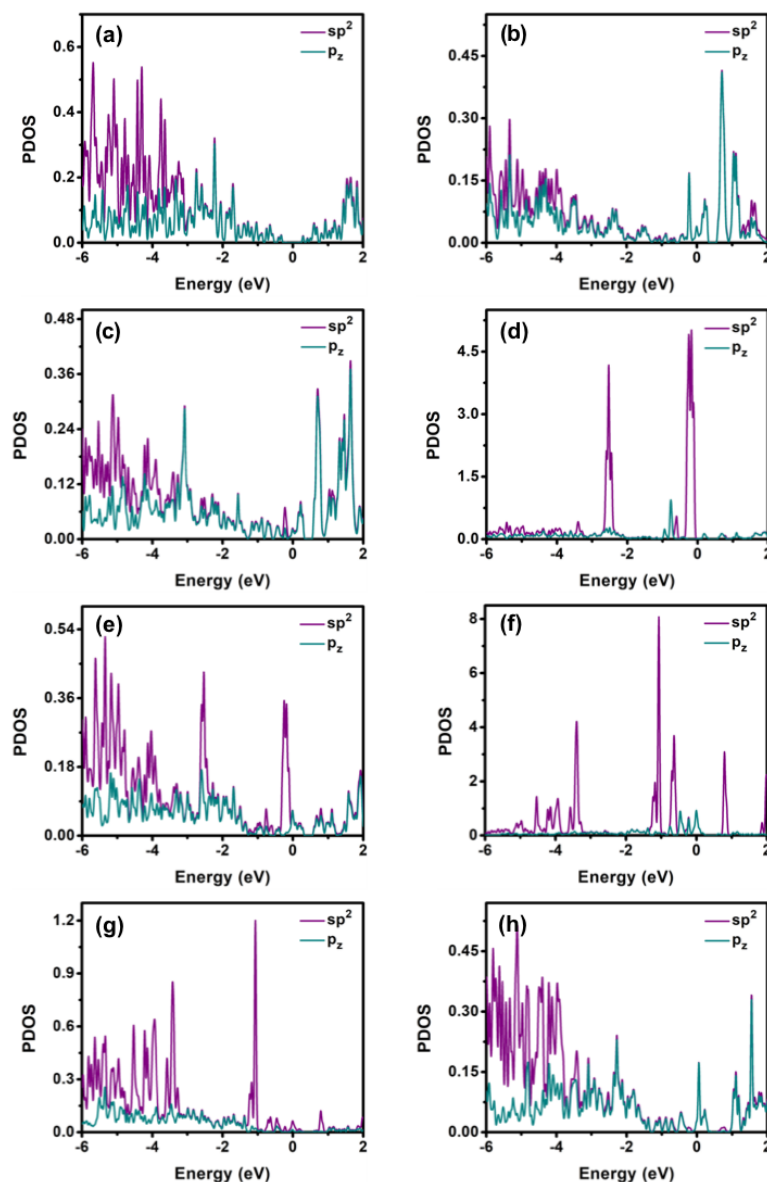
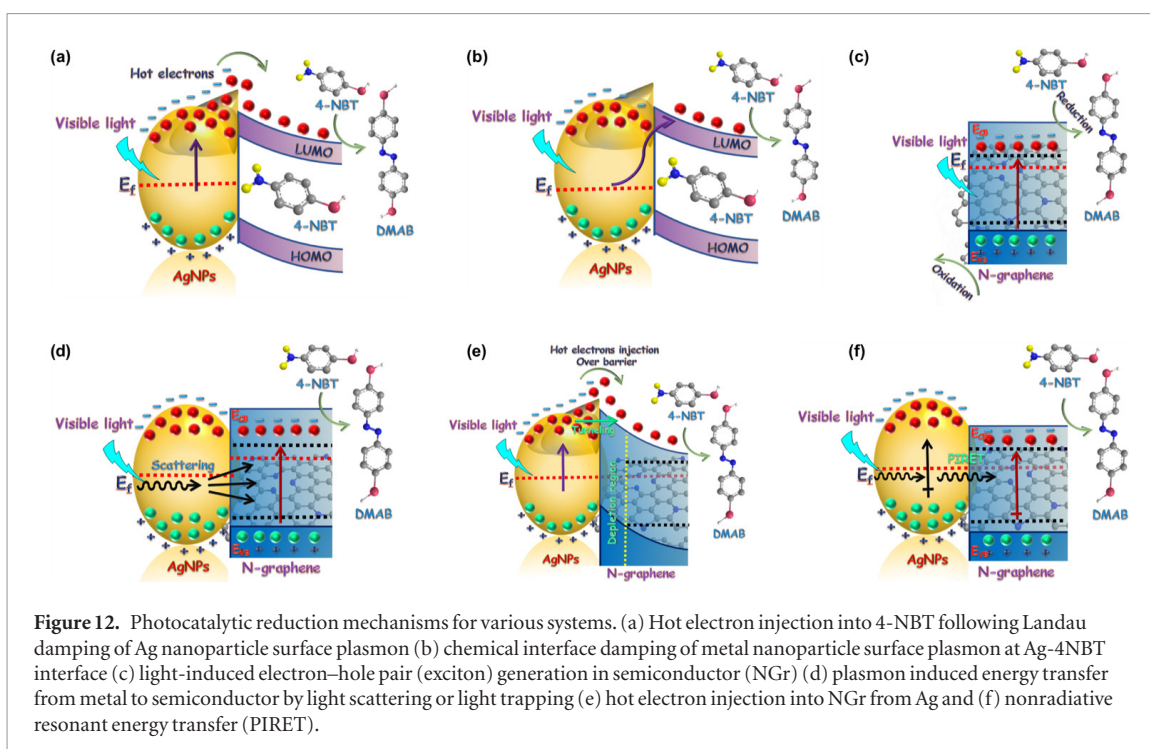


Figure 11. PDOS for selected sites of pristine graphene and N-doped graphene. Pristine graphene; (a) at a surface C atom. N-doped graphene doped with graphitic, pyridinic and pyrrolic N; (b) at a graphitic N site, (c) at a neighboring C atom of a graphitic N, (d) at a pyridinic N site, (e) at a neighboring C atom of a pyridinic N, (f) at a pyrrolic N site, (g) at a neighboring C atom of a pyrrolic N, (h) at a remote C atom from all dopant atoms.

states can directly inject electrons into adsorbate acceptor states by a process called chemical interface damping [86]. Therefore, the latter process does not require nonradiative Landau damping of plasmons to perform photocatalysis. Figures 12(a) and (b) show these two routes of photocatalytic reduction, which in our study, are primarily relevant to the case where bare Ag nanoparticles function as a stand-alone photocatalyst for the transformation of 4-NBT into DMAB. In the case of the excitonic reduction reaction, excitons are generated in bare NGr upon illumination of light, when the incident photon energy is larger than the band gap of NGr. According to the UPS result, discussed earlier in this report, NGr is a narrow bandgap semiconductor, and therefore the generation of a large number of electron–hole pairs (exciton) is likely in this material. An efficient charge separation enables the catalytic reduction of 4-NBT.

The excitonic photoreduction mechanism in NGr is shown in figure 12(c). Plasmon–exciton interaction can take place through different routes, scattering or trapping of light in semiconductor, energetic hot electron injection from plasmonic metal into the adjacent semiconductor and plasmon-induced resonant energy transfer (PIRET) [80, 87, 88]. In this project, the plexcitonic system comprising the NGr/Ag hybrid, is expected to involve these different mechanisms of charge carrier dynamics as well, even though the relative strengths might be different. Scattering or trapping of light in the semiconductor can occur after the illumination of light as a result of plasmonic metal nanoparticle induced light scattering and subsequent penetration into the adjacent semiconductor [80, 87]. This process increases the effective optical absorption cross-section and effective optical path length in the semiconductor, in addition



to local amplification of the electromagnetic field [88]. The plasmonic radiative energy transfer from metal to semiconductor is schematically drawn in figure 12(d). The plasmon decay (Landau damping) generated hot electrons in Ag nanoparticles can be directly injected into NGr conduction band. There are two possible paths available relevant to this process, the more energetic electrons, having energies greater than the Schottky barrier that forms between Ag and NGr, will be directly injected into the conduction band of NGr, while comparatively less energetic electrons can tunnel through the barrier to reach NGr [85, 89]. N-doped graphene, being a n-type semiconductor, would be expected to undergo a downward band-bending at the metal semiconductor Schottky junction, which facilitates the tunneling of hot electrons. Figure 12(e) shows the two possible ways of hot electron injection from Ag nanoparticles into NGr. However, theoretical calculation showed that efficient injection of hot electrons from plasmonic metals to adjacent semiconductors require very small nanocrystals [90]. There are other possible routes to increase the number of charge carriers in semiconductors coupled with plasmonic metal nanoparticles. The surface plasmon mediated local electromagnetic field can generate electron-hole pairs in semiconductors through a radiative process [88]. An alternate resonant energy transfer mechanism has been proposed to induce electron-hole pair generation through a nonradiative localized surface plasmon dipole relaxation [88]. This process is called PIRET [87, 88] and differs from conventional Forster-type resonance energy transfer (FRET). The incident photon energy is stored in plasmon's polarization prior to its decay or dephasing into hot electrons. This energy can be transferred to the semiconductor through the near-field interaction

[80]. PIRET process is dipole-dipole or higher order coupling mechanism in the near field, that directly excites electron-hole pairs in semiconductor through a nonradiative localized surface plasmon relaxation [88]. Figure 12(f) schematically shows the PIRET mechanism for surface photocatalytic reactions in plasmon-exciton coupled systems. Under light the electron concentration is significantly enhanced in the NGr/Ag hybrid system, as was evidenced from Raman spectroscopy and KPFM, discussed earlier in this report. 4-NBT molecules can adsorb onto Ag NPs through the thiol linkage.

Thus far, we have discussed how plasmonic metal nanoparticles coupled with semiconductor can enhance charge carriers in semiconductor and consequently enhance photocatalytic performance through three different mechanisms, far-field scattering or trapping of light in semiconductor, hot electron generation and injection into semiconductor and near-field dipole-dipole interaction mediated resonant energy transfer. For a small band gap semiconductor such as N-doped graphene, it is expected that all three mechanisms will play some role. It is reasonable to expect that scattering and near-field PIRET mechanisms are the dominant ones since there is overlap between LSPR absorption band and that of NGr (figure 2(d)). However, from figure 2(d) it is obvious that LSPR band is away from the prominent NGr absorption band located between 250 to 400 nm, which implies the absence of dominant contribution from PIRET and scattering and a significant contribution of hot electron injection mechanism in this hybrid composite system [87]. Electromagnetic simulation results (figures S7-S10, supplementary information) show larger absorption compared to scattering, indicative of a faster plasmon dephasing, supportive of hot elec-

tron transfer. Thus, our results suggest that hot electron injection could be significant in narrow band gap semiconductors, as opposed to the generally accepted fact that it is predominantly operative in wide band gap semiconductors alone.

7. Conclusion

The surface-catalyzed single-electron reduction of 4-NBMT to DMAB was used to probe the photocatalytic activity of NGr, Ag and Ngr/Ag substrates. Both the bare NGr-based excitonic photocatalyst and the plexcitonic NGr/Ag hybrid photocatalysts showed much stronger activities for the transformation of 4-NBT to DMAB in comparison to bare Ag-based plasmonic photocatalyst. Exciton-plasmon interaction leads to a synergistic enhancement of surface photocatalytic activity in the NGr/Ag plexcitonic photocatalyst. FDTD simulation results showed a sizeable electric field enhancement in the vicinity of NGr-Ag interface. Raman spectroscopic results indicated a higher charge concentration in NGr/Ag system under illumination of light. This phenomenon was in good agreement with the observations from KPFM, that showed a large surface potential reduction under light compared to in dark condition. DFT results showed that nitrogen doping of graphene produced localization of charge and created catalytically active sites with enhanced chemical reactivity at and close to the dopant atoms. The enhanced charge carrier concentration in NGr/Ag plexcitonic system holds immense potential for other photocatalytic applications.

Acknowledgments

This work was supported by the National Research Council Canada (NRC). The authors would also like to acknowledge NSERC, AITE, CMC Microsystems, Future Energy Systems, ECNU-U of A JIAST and CFI for direct and indirect support. The University of Alberta nanoFab staff member Shiau-Yin Wu is acknowledged for her help in collecting AFM data. Prof Thomas Thundat is kindly acknowledged for allowing the use of the KPFM facility. Yanan Song would like to thank the Fundamental Research Funds for the Central Universities.

ORCID iDs

Pawan Kumar  <https://orcid.org/0000-0003-2804-9298>

Ajay P Manuel  <https://orcid.org/0000-0002-5295-1057>

Ehsan Vahidzadeh  <https://orcid.org/0000-0003-1044-9576>

Sheng Zeng  <https://orcid.org/0000-0001-5153-3788>

Yanan Song  <https://orcid.org/0000-0003-1924-2598>

Karthik Shankar  <https://orcid.org/0000-0001-7347-3333>

References

- [1] Novoselov K S, Geim A K, Morozov S V, Jiang D, Katsnelson M I, Grigorieva I V, Dubonos S V and Firsov A A 2005 Two-dimensional gas of massless Dirac fermions in graphene *Nature* **438** 197–200
- [2] Allen M J, Tung V C and Kaner R B 2010 Honeycomb carbon—a review of graphene *Chem. Rev.* **110** 132–45
- [3] Ferrari A C et al 2015 Science and technology roadmap for graphene, related two-dimensional crystals, and hybrid systems *Nanoscale* **7** 4598–810
- [4] Liu H, Liu Y and Zhu D 2011 Chemical doping of graphene *J. Mater. Chem.* **21** 3335–45
- [5] Wang X, Li X, Zhang L, Yoon Y, Weber P K, Wang H, Guo J and Dai H 2009 N-doping of graphene through electrothermal reactions with ammonia *Science* **324** 768
- [6] Laref A, Ahmed A, Bin-Omran S and Luo S J 2015 First-principle analysis of the electronic and optical properties of boron and nitrogen doped carbon mono-layer graphenes *Carbon* **81** 179–92
- [7] Wang H, Maiyalagan T and Wang X 2012 Review on recent progress in nitrogen-doped graphene: synthesis, characterization, and its potential applications *ACS Catal.* **2** 781–94
- [8] Xu H, Ma L and Jin Z 2018 Nitrogen-doped graphene: synthesis, characterizations and energy applications *J. Energy Chem.* **27** 146–60
- [9] Lin C K 2018 Theoretical study of nitrogen-doped graphene nanoflakes: Stability and spectroscopy depending on dopant types and flake sizes *J. Comput. Chem.* **39** 1387–97
- [10] Lherbier A, Blase X, Niqet Y M, Triozon F and Roche S 2008 Charge transport in chemically doped 2D graphene *Phys. Rev. Lett.* **101** 036808
- [11] Kwon O H, Park S J, Hong J-Y, Han A-R, Lee J S, Lee J S, Oh J H and Jang J 2012 Flexible FET-type VEGF aptasensor based on nitrogen-doped graphene converted from conducting polymer *ACS Nano* **6** 1486–93
- [12] Chang D W et al 2013 Nitrogen-doped graphene nanoplatelets from simple solution edge-functionalization for n-type field-effect transistors *J. Am. Chem. Soc.* **135** 8981–8
- [13] Qian W, Cui X, Hao R, Hou Y and Zhang Z 2011 Facile preparation of nitrogen-doped few-layer graphene via supercritical reaction *ACS Appl. Mater. Interfaces* **3** 2259–64
- [14] Lherbier A, Botello-Mendez A R and Charlier J C 2013 Electronic and transport properties of unbalanced sublattice N-doping in graphene *Nano Lett.* **13** 1446–50
- [15] Wang Y, Shao Y, Matson D W, Li J and Lin Y 2010 Nitrogen-doped graphene and its application in electrochemical biosensing *ACS Nano* **4** 1790–8
- [16] Fan H, Li Y, Wu D, Ma H, Mao K, Fan D, Du B, Li H and Wei Q 2012 Electrochemical bisphenol a sensor based on N-doped graphene sheets *Anal. Chim. Acta* **711** 24–8
- [17] Seo S, Yoon Y, Lee J, Park Y and Lee H 2013 Nitrogen-doped partially reduced graphene oxide rewritable nonvolatile memory *ACS Nano* **7** 3607–15
- [18] Hwang J O, Park J S, Choi D S, Kim J Y, Lee S H, Lee K E, Kim Y-H, Song M H, Yoo S and Kim S O 2012 Workfunction-tunable, N-doped reduced graphene transparent electrodes for high-performance polymer light-emitting diodes *ACS Nano* **6** 159–67
- [19] Wang H, Zhang C, Liu Z, Wang L, Han P, Xu H, Zhang K, Dong S, Yao J and Cui G 2011 Nitrogen-doped graphene nanosheets with excellent lithium storage properties *J. Mater. Chem.* **21** 5430–4
- [20] Lu H et al 2017 Bottom-up synthesis of nitrogen-doped porous carbon scaffolds for lithium and sodium storage *Nanoscale* **9** 1972–7
- [21] Zhao Y, Hu C, Hu Y, Cheng H, Shi G and Qu L 2012 A versatile, ultralight, nitrogen-doped graphene framework *Angew. Chem., Int. Ed. Engl.* **51** 11371–5
- [22] Qu L, Liu Y, Baek J-B and Dai L 2010 Nitrogen-doped graphene as efficient metal-free electrocatalyst for oxygen reduction in fuel cells *ACS Nano* **4** 1321–6

- [23] Jeong H M, Lee J W, Shin W H, Choi Y J, Shin H J, Kang J K and Choi J W 2011 Nitrogen-doped graphene for high-performance ultracapacitors and the importance of nitrogen-doped sites at basal planes *Nano Lett.* **11** 2472–7
- [24] Deng Y, Tang L, Feng C, Zeng G, Wang J, Lu Y, Liu Y, Yu J, Chen S and Zhou Y 2017 Construction of plasmonic Ag and nitrogen-doped graphene quantum dots codecorated ultrathin graphitic carbon nitride nanosheet composites with enhanced photocatalytic activity: full-spectrum response ability and mechanism insight *ACS Appl. Mater. Interfaces* **9** 42816–28
- [25] Jia L, Wang D-H, Huang Y-X, Xu A-W and Yu H-Q 2011 Highly durable N-doped graphene/CdS nanocomposites with enhanced photocatalytic hydrogen evolution from water under visible light irradiation *J. Phys. Chem. C* **115** 11466–73
- [26] Ding Q, Shi Y, Chen M, Li H, Yang X, Qu Y, Liang W and Sun M 2016 Ultrafast dynamics of plasmon–exciton interaction of Ag nanowire–graphene hybrids for surface catalytic reactions *Sci. Rep.* **6** 32724
- [27] Dong B, Fang Y, Chen X, Xu H and Sun M 2011 Substrate-, wavelength-, and time-dependent plasmon-assisted surface catalysis reaction of 4-nitrobenzenethiol dimerizing to p,p'-dimercaptoazobenzene on Au, Ag, and Cu films *Langmuir* **27** 10677–82
- [28] Ding Q, Li R, Chen M and Sun M 2017 Ag nanoparticles–TiO₂ film hybrid for plasmon–exciton co-driven surface catalytic reactions *Appl. Mater. Today* **9** 251–8
- [29] Yang X, Yu H, Guo X, Ding Q, Pullerits T, Wang R, Zhang G, Liang W and Sun M 2017 Plasmon–exciton coupling of monolayer MoS₂–Ag nanoparticles hybrids for surface catalytic reaction *Mater. Today Energy* **5** 72–8
- [30] Wu H-Y, Lai Y-H, Hsieh M-S, Lin S-D, Li Y-C and Lin T-W 2014 Highly intensified surface enhanced Raman Scattering through the formation of p,p'-dimercaptoazobenzene on Ag nanoparticles/graphene oxide nanocomposites *Adv. Mater. Interfaces* **1** 1400119
- [31] Manuel A P, Kirkey A, Mahdi N and Shankar K 2019 Plexitronics—fundamental principles and optoelectronic applications *J. Mater. Chem. C* **7** 1821–53
- [32] Achermann M 2010 Exciton–plasmon interactions in metal-semiconductor nanostructures *J. Phys. Chem. Lett.* **1** 2837–43
- [33] Kumar P, Boukherroub R and Shankar K 2018 Sunlight-driven water-splitting using two-dimensional carbon based semiconductors *J. Mater. Chem. A* **6** 12876–931
- [34] Zeng B, Xia Q and Zeng W 2019 Fabrication and characterization of novel graphene/iodine doped CdS nanoplates and their photocatalytic performances *J. Mater. Sci., Mater. Electron.* **30** 11619–26
- [35] Zeng B, Liu W, Zeng W and Jin C 2018 A general method for the synthesis of graphene–metal sulphide nanosheets *J. Nanopart. Res.* **20** 55
- [36] Singh D K, Iyer P K and Giri P K 2011 Improved chemical synthesis of graphene using a safer solvothermal route *Int. J. Nanosci.* **10** 39–42
- [37] Rajender G, Kumar J and Giri P K 2018 Interfacial charge transfer in oxygen deficient TiO₂–graphene quantum dot hybrid and its influence on the enhanced visible light photocatalysis *Appl. Catal. B* **224** 960–72
- [38] Giglio C S, Osazuwa O, Kontopoulou M and Docoslis A 2019 Achieving high yield of graphene nanoplatelets in poloxamer-assisted ultrasonication of graphite in water *J. Colloid Interface Sci.* **539** 107–17
- [39] Liu B, Yang C M, Liu Z W and Lai C S 2017 N-doped graphene with low intrinsic defect densities via a solid source doping technique *Nanomaterials* **7** 302
- [40] Liu Q B, Yu C, He Z Z, Gu G D, Wang J J, Zhou C J, Guo J C, Gao X D and Feng Z H 2018 Chemical vapor deposition graphene of high mobility by gradient growth method on an 4H-SiC (000 1) substrate *Appl. Surf. Sci.* **454** 68–73
- [41] Li X *et al* 2009 Large-area synthesis of high-quality and uniform graphene films on copper foils *Science* **324** 1312
- [42] Li X, Zhu Y, Cai W, Borysiak M, Han B, Chen D, Piner R D, Colombo L and Ruoff R S 2009 Transfer of large-area graphene films for high-performance transparent conductive electrodes *Nano Lett.* **9** 4359–63
- [43] Siekkinen A R, McLellan J M, Chen J and Xia Y 2006 Rapid synthesis of small silver nanocubes by mediating polyol reduction with a trace amount of sodium sulfide or sodium hydrosulfide *Chem. Phys. Lett.* **432** 491–6
- [44] Chen C, Wang L, Yu H, Wang J, Zhou J, Tan Q and Deng L 2007 Morphology-controlled synthesis of silver nanostructures via a seed catalysis process *Nanotechnology* **18** 115612
- [45] You T, Jiang L, Yin P, Shang Y, Zhang D, Guo L and Yang S 2014 Direct observation of p,p'-dimercaptoazobenzene produced from p-aminothiophenol and p-nitrothiophenol on Cu₂O nanoparticles by surface-enhanced Raman spectroscopy *J. Raman Spectrosc.* **45** 7–14
- [46] Shen C C, Tseng C C, Lin C T, Li L J and Liu H L 2014 Optical properties of nitrogen-doped graphene thin films probed by spectroscopic ellipsometry *Thin Solid Films* **571** 675–9
- [47] Mohammadi A, Nicholls D L and Docoslis A 2018 Improving the surface-enhanced Raman scattering performance of silver nanodendritic substrates with sprayed-on graphene-based coatings *Sensors* **18** 3404
- [48] Wu W, Wu M, Sun Z, Li G, Ma Y, Liu X, Wang X and Chen X 2013 Morphology controllable synthesis of silver nanoparticles: optical properties study and SERS application *J. Alloys Compd.* **579** 117–23
- [49] Nogueira A L, Machado R A F, de Souza A Z, Martinello F, Franco C V and Dutra G B 2014 Synthesis and characterization of silver nanoparticles produced with a bifunctional stabilizing agent *Ind. Eng. Chem. Res.* **53** 3426–34
- [50] Luo Z, Lim S, Tian Z, Shang J, Lai L, MacDonald B, Fu C, Shen Z, Yu T and Lin J 2011 Pyridinic N doped graphene: synthesis, electronic structure, and electrocatalytic property *J. Mater. Chem.* **21** 8038–44
- [51] Cançado L G, Takai K, Enoki T, Endo M, Kim Y A, Mizusaki H, Jorio A, Coelho L N, Magalhães-Paniago R and Pimenta M A 2006 General equation for the determination of the crystallite size La of nanographite by Raman spectroscopy *Appl. Phys. Lett.* **88** 163106
- [52] Zhang C, Fu L, Liu N, Liu M, Wang Y and Liu Z 2011 Synthesis of nitrogen-doped graphene using embedded carbon and nitrogen sources *Adv. Mater.* **23** 1020–4
- [53] Ni Z H, Wang H M, Kasim J, Fan H M, Yu T, Wu Y H, Feng Y P and Shen Z X 2007 Graphene thickness determination using reflection and contrast spectroscopy *Nano Lett.* **7** 2758–63
- [54] Das A *et al* 2008 Monitoring dopants by Raman scattering in an electrochemically top-gated graphene transistor *Nat. Nanotechnol.* **3** 210–5
- [55] Biroju R K and Giri P K 2014 Defect enhanced efficient physical functionalization of graphene with gold nanoparticles probed by resonance Raman spectroscopy *J. Phys. Chem. C* **118** 13833–43
- [56] Mahmoud M A, Tabor C E and El-Sayed M A 2009 Surface-enhanced Raman scattering enhancement by aggregated silver nanocube monolayers assembled by the Langmuir–Blodgett technique at different surface pressures *J. Phys. Chem. C* **113** 5493–501
- [57] Xu J, Wang M, Wickramaratne N P, Jaroniec M, Dou S and Dai L 2015 High-performance sodium ion batteries based on a 3D anode from nitrogen-doped graphene foams *Adv. Mater.* **27** 2042–8
- [58] Zhang Y, Fugane K, Mori T, Niu L and Ye J 2012 Wet chemical synthesis of nitrogen-doped graphene towards oxygen reduction electrocatalysts without high-temperature pyrolysis *J. Mater. Chem.* **22** 6575–80
- [59] Van Khai T, Na H G, Kwak D S, Kwon Y J, Ham H, Shim K B and Kim H W 2012 Significant enhancement of blue emission and electrical conductivity of N-doped graphene *J. Mater. Chem.* **22** 17992–8003
- [60] Zhang H, Kuila T, Kim N H, Yu D S and Lee J H 2014 Simultaneous reduction, exfoliation, and nitrogen doping of graphene oxide via a hydrothermal reaction for energy storage electrode materials *Carbon* **69** 66–78
- [61] Kumar P, Mungse H P, Khatra O P and Jain S L 2015 Nitrogen-doped graphene-supported copper complex: a novel photocatalyst for CO₂ reduction under visible light irradiation *RSC Adv.* **5** 54929–35

- [62] Geng D, Chen Y, Chen Y, Li Y, Li R, Sun X, Ye S and Knights S 2011 High oxygen-reduction activity and durability of nitrogen-doped graphene *Energy Environ. Sci.* **4** 760–4
- [63] Reddy A L M, Srivastava A, Gowda S R, Gullapalli H, Dubey M and Ajayan P M 2010 Synthesis of nitrogen-doped graphene films for lithium battery application *ACS Nano* **4** 6337–42
- [64] Sandoval S, Kumar N, Oro-Solé J, Sundaresan A, Rao C N R, Fuertes A and Tobias G 2016 Tuning the nature of nitrogen atoms in N-containing reduced graphene oxide *Carbon* **96** 594–602
- [65] Zhang P, Shao C, Zhang Z, Zhang M, Mu J, Guo Z and Liu Y 2011 *In situ* assembly of well-dispersed Ag nanoparticles (AgNPs) on electrospun carbon nanofibers (CNFs) for catalytic reduction of 4-nitrophenol *Nanoscale* **3** 3357–63
- [66] Xia H, Hong C, Shi X, Li B, Yuan G, Yao Q and Xie J 2015 Hierarchical heterostructures of Ag nanoparticles decorated MnO₂ nanowires as promising electrodes for supercapacitors *J. Mater. Chem. A* **3** 1216–21
- [67] Schwierz F 2010 Graphene transistors *Nat. Nanotechnol.* **5** 487–96
- [68] Kondo T et al 2012 Atomic-scale characterization of nitrogen-doped graphite: effects of dopant nitrogen on the local electronic structure of the surrounding carbon atoms *Phys. Rev. B* **86** 035436
- [69] Schiros T et al 2012 Connecting dopant bond type with electronic structure in N-doped graphene *Nano Lett.* **12** 4025–31
- [70] Melitz W, Shen J, Kummel A C and Lee S 2011 Kelvin probe force microscopy and its application *Surf. Sci. Rep.* **66** 1–27
- [71] Wu M-C, Liao H-C, Cho Y-C, Tóth G, Chen Y-F, Su W-F and Kordás K 2013 Photo-Kelvin probe force microscopy for photocatalytic performance characterization of single filament of TiO₂ nanofiber photocatalysts *J. Mater. Chem. A* **1** 5715–20
- [72] Spadafora E J, Demadrille R, Ratier B and Grevin B 2010 Imaging the carrier photogeneration in nanoscale phase segregated organic heterojunctions by Kelvin probe force microscopy *Nano Lett.* **10** 3337–42
- [73] Li D B, Sun X J, Jia Y P, Stockman M I, Paudel H P, Song H, Jiang H and Li Z M 2017 Direct observation of localized surface plasmon field enhancement by Kelvin probe force microscopy *Light Sci. Appl.* **6** e17038
- [74] Sun M and Xu H 2012 A novel application of plasmonics: plasmon-driven surface-catalyzed reactions *Small* **8** 2777–86
- [75] Xu P, Kang L, Mack N H, Schanze K S, Han X and Wang H L 2013 Mechanistic understanding of surface plasmon assisted catalysis on a single particle: cyclic redox of 4-aminothiophenol *Sci. Rep.* **3** 2997
- [76] Huang Y F, Zhang M, Zhao L B, Feng J M, Wu D Y, Ren B and Tian Z Q 2014 Activation of oxygen on gold and silver nanoparticles assisted by surface plasmon resonances *Angew. Chem., Int. Ed. Engl.* **53** 2353–7
- [77] Lin W, Cao Y, Wang P and Sun M 2017 Unified treatment for plasmon–exciton Co-driven reduction and oxidation reactions *Langmuir* **33** 12102–7
- [78] Dong B, Fang Y, Xia L, Xu H and Sun M 2011 Is 4-nitrobenzenethiol converted to p,p'-dimercaptoazobenzene or 4-aminothiophenol by surface photochemistry reaction? *J. Raman Spectrosc.* **42** 1205–6
- [79] Canpean V, Iosin M and Astilean S 2010 Disentangling SERS signals from two molecular species: a new evidence for the production of p,p'-dimercaptoazobenzene by catalytic coupling reaction of p-aminothiophenol on metallic nanostructures *Chem. Phys. Lett.* **500** 277–82
- [80] Cushing S K and Wu N 2016 Progress and perspectives of plasmon-enhanced solar energy conversion *J. Phys. Chem. Lett.* **7** 666–75
- [81] Kohn W and Sham L J 1965 Self-consistent equations including exchange and correlation effects *Phys. Rev.* **140** A1133–8
- [82] Ozaki T 2003 Variationally optimized atomic orbitals for large-scale electronic structures *Phys. Rev. B* **67** 155108
- [83] Perdew J P, Burke K and Ernzerhof M 1996 Generalized gradient approximation made simple *Phys. Rev. Lett.* **77** 3865–8
- [84] Zhang L and Xia Z 2011 Mechanisms of oxygen reduction reaction on nitrogen-doped graphene for fuel cells *J. Phys. Chem. C* **115** 11170–6
- [85] Moskovits M 2011 Hot electrons cross boundaries *Science* **332** 676
- [86] Kale M J, Avanesian T and Christopher P 2013 Direct photocatalysis by plasmonic nanostructures *ACS Catal.* **4** 116–28
- [87] Wu N 2018 Plasmonic metal-semiconductor photocatalysts and photoelectrochemical cells: a review *Nanoscale* **10** 2679–96
- [88] Cushing S K, Li J, Meng F, Senty T R, Suri S, Zhi M, Li M, Bristow A D and Wu N 2012 Photocatalytic activity enhanced by plasmonic resonant energy transfer from metal to semiconductor *J. Am. Chem. Soc.* **134** 15033–41
- [89] Shiraishi Y, Yasumoto N, Imai J, Sakamoto H, Tanaka S, Ichikawa S, Ohtani B and Hirai T 2017 Quantum tunneling injection of hot electrons in Au/TiO₂ plasmonic photocatalysts *Nanoscale* **9** 8349–61
- [90] Govorov A O, Zhang H and Gun'ko Y K 2013 Theory of photoinjection of hot plasmonic carriers from metal nanostructures into semiconductors and surface molecules *J. Phys. Chem. C* **117** 16616–31